1   **REVISION 1**

2

3   **Constraints on iron sulfate and iron oxide mineralogy from ChemCam visible/near-**

4   **infrared reflectance spectroscopy of Mt. Sharp basal units, Gale Crater, Mars**

5

6   Jeffrey R. Johnson[1], James F. Bell III[2], Steve Bender[3], Diana Blaney[4], Edward Cloutis[5], Bethany

7   Ehlmann[4,6], Abigail Fraeman[6], Olivier Gasnault[7], Kjartan Kinch[8], Stéphane Le Mouélic[9],

8   Sylvestre Maurice[7], Elizabeth Rampe[11], David Vaniman[3], Roger C. Wiens[10]

9

10

11   1—Johns Hopkins University Applied Physics Laboratory, Laurel, MD
12   2—Arizona State University, Tempe, AZ
13   3—Planetary Science Institute, Tucson, AZ
14   4—Jet Propulsion Laboratory, Pasadena, CA
15   5—University of Winnipeg, Winnipeg, Manitoba, Canada
16   6—California Institute of Technology, Pasadena, CA
17   7—Université de Toulouse, CNRS, Institut de Recherche en Astrophysique et Planetologie,
18   Toulouse, France
19   8—University of Copenhagen, Niels Bohr Institute, Copenhagen, Denmark
20   9—Université de Nantes, Laboratoire de Planétologie et Géodynamique, Nantes, France
21   10—Los Alamos National Laboratory, Los Alamos, NM
22   11—Johnson Space Center, Houston, TX

23

24

28   Jeffrey.r.johnson@jhuapl.edu
29   Jim.bell@asu.edu
30   sbender@psi.edu
31   diana.l.blaney@jpl.nasa.gov
32   ehlmann@caltech.edu
33   afraeman@caltech.edu
34   Olivier.Gasnault@irap.omp.eu
35   kinch@nbi.ku.dk
36   stephane.lemouelic@univ-nantes.fr
37   sylvestre.maurice@irap.omp.eu
38   elizabeth.b.rampe@nasa.gov
39   dvaniman@psi.edu
40   rwiens@lanl.gov

41

42

2

ABSTRACT

43

44 Relative reflectance point spectra (400-840 nm) were acquired by the Chemistry and Camera

45 (ChemCam) instrument on the Mars Science Laboratory (MSL) rover Curiosity in passive mode

46 (no laser) of drill tailings and broken rock fragments near the rover as it entered the lower

47 reaches of Mt. Sharp and of landforms at distances of 2-8 kilometers. Freshly disturbed surfaces

48 are less subject to the spectral masking effects of dust, and revealed spectral features consistent

49 with the presence of iron oxides and ferric sulfates. We present the first detection on Mars of a

50 ~433 nm absorption band consistent with small abundances of ferric sulfates, corroborated by

51 jarosite detections by the Chemistry and Mineralogy (CheMin) X-ray diffraction instrument in

52 the Mojave, Telegraph Peak, and Confidence Hills drilled samples. Disturbed materials near the

53 Bonanza King region also exhibited strong 433 nm bands and negative near-infrared spectral

54 slopes consistent with jarosite. ChemCam passive spectra of the Confidence Hills and Mojave

55 drill tailings showed features suggestive of the crystalline hematite identified by CheMin

56 analyses. The Windjana drill sample tailings exhibited flat, low relative reflectance spectra,

57 explained by the occurrence of magnetite detected by CheMin. Passive spectra of Bonanza King

58 were similar, suggesting the presence of spectrally dark and neutral minerals such as magnetite.

59 Long-distance spectra of the "Hematite Ridge" feature (3-5 km from the rover) exhibited

60 features consistent with crystalline hematite. The Bagnold dune field north of the Hematite Ridge

61 area exhibited low relative reflectance and near-infrared features indicative of basaltic materials

62 (olivine, pyroxene). Light-toned layers south of Hematite Ridge lacked distinct spectral features

63 in the 400-840 nm region, and may represent portions of nearby clay minerals and sulfates

64 mapped with orbital near-infrared observations. The presence of ferric sulfates such as jarosite in

65 the drill tailings suggests a relatively acidic environment, likely associated with flow of iron-

66   bearing fluids, associated oxidation, and/or hydrothermal leaching of sedimentary rocks.

67   Combined with other remote sensing data sets, mineralogical constraints from ChemCam passive

68   spectra will continue to play an important role in interpreting the mineralogy and composition of

69   materials encountered as Curiosity traverses further south within the basal layers of the Mt.

70   Sharp complex.

71   **Keywords**: Mars spectroscopy, Mars remote sensing, visible/near-infrared, IR Spectroscopy,

72   ferric sulfates, iron oxides

73

<div align="center">

INTRODUCTION

</div>

74

75   During the first 1000 martian days (sols) of operations the Mars Science Laboratory (MSL)

76 rover Curiosity encountered a diverse array of stratigraphic settings within the 154 km diameter

77 Gale Crater. These included ancient systems of groundwater networks, sporadic streams, and

78 ephemeral lakes considered to represent potential habitable environments (Williams et al. 2013;

79 Grotzinger et al. 2014, 2015a,b; Vasavada et al. 2014). Although the majority of the sediments

80 associated with these alluvial, fluvial, and/or deltaic systems were largely composed of primary

81 igneous minerals, detailed chemical and mineralogical analyses demonstrated that chemical

82 weathering and/or diagenetic aqueous alteration occurred at a variety of pH levels (Schmidt et al.

83 2014; Sautter et al. 2014; Bish et al. 2014; Vaniman et al. 2014). Iron oxides, calcium and ferric

84 sulfates, hydrated clay minerals, as well as substantial proportions of amorphous materials have

85 been measured in drilled samples (Ming et al. 2014; Treiman et al. 2014; Vaniman et al. 2014;

86 McClennan et al. 2014; Bish et al. 2014; Nachon et al. 2014; Bristow et al. 2015). Orbital

87 mineralogical mapping of Gale Crater using visible/near-infrared reflectance spectroscopy also

88 demonstrated that rock layers at the base of the ~ 5 km high Mt. Sharp (Aeolis Mons) contained

89 appreciable amounts of clay minerals, sulfates, silica, and hematite, likely related to early

90 climatic changes (Anderson and Bell 2010; Milliken et al. 2010; Grotzinger and Milliken 2012;

91 Fraeman et al. 2013, Wray, 2013; Seelos et al. 2014). Indeed, the presence and distribution of

92 ferric sulfates (such as jarosite) and iron oxides (such as hematite and magnetite) detected by

93 Curiosity are particularly important in constraining the aqueous diagenetic history of rocks along

94 the rover traverse, and the geochemical and temperature history of near-surface fluids that

95 interacted with these rocks (e.g., Dixon et al. 2015).

<div align="center">

5

</div>

96   During the MSL mission elemental composition has been obtained for in-situ samples using

97   the Alpha Particle X-ray Spectrometer (APXS; Schmidt et al., 2013) and remotely using Laser-

98   Induced Breakdown Spectroscopy (LIBS) with the Chemistry and Camera (ChemCam)

99   instrument (e.g., Wiens et al. 2013, 2015). Mineralogy has been determined for a few drilled

100   samples using the Chemistry and Mineralogy (CheMin) powder x-ray diffraction instrument. For

101   the vast majority of rocks and soils not directly ingested by the rover's drilling and sampling

102   system, additional constraints on mineralogy and composition were obtained using visible/near-

103   infrared (VNIR) reflectance spectroscopy (400-1000 nm) with two complementary methods:

104   point spectroscopy (400-840 nm) via the passive mode of ChemCam (Johnson et al. 2015), and

105   multispectral imaging (445-1010 nm) from the Mastcam stereo camera system (Bell et al. 2013;

106   Rice et al. 2013; Wellington et al. 2014). Because the MSL landing site region is relatively dusty

107   (e.g., Seelos et al. 2014, Ehlmann and Buz 2015), many pristine surfaces exhibit VNIR spectra

108   consistent with variable amounts of dust cover. However, freshly disturbed surfaces (drill tailing

109   fines, areas subjected to rover wheels) are less subject to the masking effects of such dust.

110   In this paper we present ChemCam VNIR spectra of drill tailings and nearby exposed

111   materials to demonstrate the presence of iron oxides such as hematite and magnetite, and we

112   document the first detection on Mars of the ~433 nm absorption band associated with ferric

113   sulfates. We also present long-distance results that demonstrate the capability to detect hematite

114   and variable spectral properties of outcrop and dune materials several kilometers away. We

115   compare ChemCam spectra to laboratory spectra of various minerals and to mineralogical results

116   from CheMin (e.g., Bish et al. 2014; Downs et al. 2015). In a companion paper, Wellington et al.

117   (this issue) present Mast Camera (Mastcam) multispectral imaging results for similar targets,

118   employing the longer wavelengths and greater spatial coverage provided by Mastcam.

119

120   **BACKGROUND**

121   **VNIR Spectroscopy**

122   Visible/near-infrared (400-1000 nm) spectra provide a valuable means of constraining

123   mineralogy and crystallinity of iron-bearing minerals on Mars and in the laboratory (e.g., Singer

124   et al. 1979; Morris et al., 2000; Bell et al. 2000, 2008; Johnson et al. 2007; Ehlmann and

125   Edwards, 2014).   A decrease in reflectance towards the near-infrared is attributable to the

126   presence of Fe^{2+} absorption bands associated with mafic silicate minerals such as pyroxenes and

127   olivine (e.g., Roush et al. 1993). Absorptions from Fe^{3+} cause strong, positive slopes from the

128   blue to red wavelengths, with relative reflectance maxima typically near 750 nm.   Ratios of

129   red/blue wavelengths provide first-order information on the relative level of oxidation of surface

130   materials and/or degree of dust coatings on martian surfaces (e.g., Johnson and Grundy 2001;

131   Johnson et al. 2003). Relatively dust-free "gray" rocks observed by in situ multispectral imagers

132   on Mars exhibit lower red/blue color ratios than more dust-coated surfaces (McSween et al.

133   1999; Bell et al. 2004a,b; Farrand et al. 2006, 2007, 2008a,b; Wellington et al, this issue). The

134   strength of the short wavelength Fe^{3+} absorption edge can be determined by the spectral

135   curvature near 600 nm. Absorptions near 535 nm and in the 800-1000 nm region are consistent

136   with the presence of crystalline ferric oxides such as hematite (Morris et al. 1985, 1997, 2000;

137   Bell et al. 2004a,b;). Ferric sulfates such as jarosite, coquimbite, and rhomboclase also exhibit

138   absorption bands near 433 nm, sometimes with weaker 530, 790, and/or ~870 nm bands (Bishop

139   and Murad, 1996; Bishop et al. 2015; Johnson et al. 2007; Lane et al. 2008). The ~433 nm band

140   is related to the $^{6}A_{1g}$-($^{4}A_{1g}$,$^{4}E_{g}$) ferric iron spin-forbidden crystal field transition, where the shape

141   and position of this band are related to the distortion of the iron octahedra (Rossman et al. 1975;

142   Sherman et al. 1982; Cloutis et al. 2006a, 2008; McCollom et al. 2014; Sklute et al. 2015) and to

143   a lesser extent grain size (Pitman et al. 2014).

ChemCam Passive Spectroscopy

145   The LIBS portion of the ChemCam instrument disperses light emitted from a laser-

146   generated plasma onto three spectrometers to detect elemental emission lines at high spectral (<

147   1 nm) and spatial (0.65 mrad FOV) resolution (Wiens et al. 2013, 2015). Johnson et al. (2015)

148   demonstrated that although the ChemCam "violet" (VIO, 382-469 nm) and visible/near-infrared

149   (VNIR, 474-906 nm) spectrometers were not designed for reflectance spectroscopy, they

150   exhibited sufficient sensitivity to allow collection of useful surface spectral reflectance in passive

151   mode (i.e., without using the laser). Johnson et al. (2015) presented relative reflectance spectra

152   (400-840 nm) of rocks, dust, and soils near the rover (~2-7 m) acquired during the first 360 sols,

153   where spatial resolutions of the point locations ranged from 1.3-4.5 mm. Analyses of the band

154   depths, spectral slopes, and ratios among these spectra revealed six spectral endmembers

155   characterized by variations in ferrous and ferric components. For example, "exposed" materials

156   (brushed or freshly broken surfaces) exhibited low 535 nm band depths and low 670/440 nm

157   ratios, indicative of the less oxidized nature of these more ferrous materials relative to, e.g.,

158   Martian dust. Typical reddish, oxidized, dusty surfaces exhibited similarities to palagonite-rich

159   soils. "Dark" float rocks exhibited low relative reflectance and significant downturns longward

160   of 700 nm that were consistent with the presence of orthopyroxene. Magnesium-rich "raised

161   ridges" tended to exhibit distinct, negative near-infrared slopes. Calcium-sulfate veins exhibited

162   the highest relative reflectances, but were still relatively red owing to the effects of dust and/or

163   minor structural Fe^{3+} contamination. Such dust was less prominent on rocks within the "blast

164   zone" surrounding the Bradbury landing site. These samples were likely affected by the landing

165   thrusters, which partially removed the ubiquitous dust coatings.

166

167   **METHODOLOGY**

168   For every LIBS point measurement acquired by ChemCam with its laser, a 3 msec

169   exposure passive ("dark") measurement is acquired without the laser for calibration purposes. As

170   shown by Johnson et al. (2015) these "dark" measurements are of sufficient quality to be used as

171   passive radiance spectra when acquired on sunlit surfaces. Longer exposure ("dedicated")

172   measurements at 30 msec were acquired when possible for specific targets of interest to increase

173   the signal to noise ratio (SNR). Calibration of such measurements to relative reflectance

174   followed procedures similar to those established for field spectroscopy (e.g., Johnson et al. 2001;

175   Milton et al. 2009), in which a scene radiance spectrum is divided by a calibration target radiance

176   spectrum. We used observations acquired at 3 msec and 30 msec exposures on Sol 76 of the

177   white ChemCam calibration target holder to minimize dark current variations between scene and

178   calibration targets. We converted the raw data to radiance using the methods described by

179   Johnson et al. (2015). The ratio of the scene and calibration target radiance measurements,

180   multiplied by the known laboratory reflectance of the calibration target material (Wiens et al.

181   2013), provided an estimate of relative reflectance. Johnson et al. (2015) estimated that the

182   radiance absolute calibration uncertainty was 6-8%. They noted that even with moderate relative

183   reflectance uncertainties (e.g., 20-30%), the band positions and shapes were resilient to

184   calibration errors and ultimately useful in constraining compositions and/or mineral detections.

185   Remote Micro-Imager (RMI) images were acquired as part of ChemCam observations,

186   from which accurate locations for the individual points within a raster could be placed (Wiens et

9

187   al. 2012, 2015; Maurice et al. 2012; Le Mouélic et al. 2015). Comparison to Mastcam M-100

188   images acquired as part of the ChemCam observations also provided context images for

189   interpreting the passive spectra. The 0.65 mrad FOV of the spectra corresponds to a ~ 2mm spot

190   size at an observation distance of 3 mm. Longer-distance observation effective FOVs are subject

191   to minor, variable elongation resulting from the projection of the FOV onto local topography.

192   Analyses of the spectra benefited from the use of spectral parameters calculated using ±5

193   nm averages around a central wavelength. In the visible wavelengths, 670/440 nm ratios are

194   sensitive to oxidation state and/or dust deposition, whereas in the near-infrared region slopes

195   from 750 nm to 840 nm and 600 nm to 840 nm are indicative of the strength of iron absorptions.

196   The 600 nm band depth (shoulder) is sensitive to the strength of the short wavelength ferric

197   oxide absorption edge, and was calculated with a continuum between 535 nm and 670 nm. The

198   535 nm band depth is sensitive to the presence of crystalline ferric oxides (e.g., Morris et al.

199   1997, 2000) and was calculated with a continuum between 500 nm and 600 nm (cf. Bell et al.

200   2000).

201   **DATA SETS**

202   The primary data sets used here and their observation sequence identifications are listed

203   in Table 1. They include representative samples of the drill tailings from Cumberland (at

204   Yellowknife Bay), Windjana (at The Kimberley), and the triad of samples collected in the

205   Pahrump Hills area (in stratigraphic order, upsection: Confidence Hills, Mojave, and Telegraph

206   Peak). Figure 1b shows their locations on a rover traverse map, in addition to two targets of

207   interest near Hidden Valley: Bonanza King and Perdido2. All spectra examined here were

208   acquired with dedicated 30 msec exposures except for 3 msec exposures (used as part of the

209   standard LIBS passive background measurements) for Cumberland, Windjana, and Confidence

210   Hills. Also listed in Table 1 are long distance passive spectra sequences acquired of landforms

211   2-8 km south of the rover's traverse. These areas encompassed dark-toned, dominantly basaltic

212   dunes, hematite-bearing materials on the region informally known as Hematite Ridge (Fraeman

213   et al. 2013), fan-like materials occurring near the base of Mt. Sharp (Figure 1a), and nearby light-

214   toned mounds. Table 1 also includes the atmospheric opacity values calculated from Mastcam

215   observations at 880 nm using the techniques of Lemmon et al. (2004), as well as the time of day

216   and phase angle of the observations.

217   **Drill Tailings and Disturbed Materials**

218   **Cumberland**. The two drill samples acquired at Yellowknife Bay were John Klein and

219   Cumberland. CheMin results showed each to have similar mineralogy in their crystalline

220   components with dominantly plagioclase feldspar (22 wt%), pyroxene (16 wt%), clay minerals

221   (~20% trioctahedral smectites), magnetite (4 wt%), minor calcium sulfates, iron

222   oxide/hydroxides, and Fe-sulfides, and ~30 wt% amorphous materials (e.g., Vaniman et al.

223   2014). Although the passive spectra of each drill sample were essentially identical, the

224   Cumberland data were acquired earlier in the day (at lower detector temperatures) and therefore

225   exhibited slight better SNR. As such, we used the Cumberland data from Sol 289 in this work.

226   **Windjana**. Figure 2 shows the RMI image and location of 8 raster points acquired on Sol 619

227   of the Windjana mini-drill tailings in The Kimberley region (cf. Fig. 1a). The full drill tailings

228   (shown in the accompanying Mastcam image) exhibited identical reflectance properties.

229   CheMin results for the Windjana crystalline components were modeled as augite (20 wt%),

230   pigeonite (10 wt%), olivine (5 wt%), monoclinic sanidine (20 wt%), plagioclase (4 wt%)

231   magnetite (12 wt%), phyllosilicate (8 wt%), and amorphous /poorly crystalline phases (15-20

232   wt%). (e.g., Downs et al. 2015; Treiman et al. 2015a,b).

11

233   **Bonanza King and Perdido2**. Near the entrance to Hidden Valley drilling was attempted on

234   the Bonanza King target, but abandoned after the target became unstable during the mini-drill

235   attempt (Anderson et al. 2015b). Figure 3 includes the Sol 726 RMI mosaic showing the

236   locations of a 4x4 raster and the Mastcam image of this disturbed area. Although no CheMin

237   analyses were obtained of this material, the APXS and ChemCam LIBS data indicated a

238   dominantly basaltic composition with minor calcium sulfates. Compared to Windjana and the

239   Yellowknife Bay samples, the Fe and Mg were lower, Si higher, with an unusually high amount

240   of P (P_2O_5~2%) (Thompson et al. 2015).   While at this location ChemCam 3 msec passive

241   spectra were acquired of a freshly broken rock fragment named Perdido that suggested

242   interesting spectral features. Therefore, a dedicated passive raster (30 msec exposures) at the

243   same location was collected on Sol 728. Figure 4 shows the RMI and Mastcam images of these

244   targets, in which the 5th location of the passive raster was located on the surface of a broken

245   fragment named Perdido2.

246   **Confidence Hills**. At Pahrump Hills the Confidence Hills drill tailings were observed on Sol

247   762 after the full drilling was completed. Figure 5 shows the 1x10 raster on the RMI mosaic and

248   accompanying Mastcam image of the target Stovepipe Wells, where locations #4 through #10

249   were located on the drill tailings. CheMin crystalline phases include plagioclase (26 wt%),

250   augite (7 wt%), pigeonite (7 wt%), forsterite (<1 wt%), hematite (8 wt%), magnetite (4 wt%),

251   potassium feldspar (6 wt%), phyllosilicate (10 wt%), trace (~1 wt %) cristobalite, ilmenite,

252   jarosite, and quartz, and amorphous material comprising 26 wt% of the sample (cf. Cavanagh et

253   al. 2015; Rampe et al. 2015a).

254   **Mojave**. The mini-drill attempt at Mojave was partially successful, as evidenced by Figure 6,

255   which shows an RMI mosaic and 1x5 dedicated passive raster acquired on Sol 869 with an

12

256   accompanying Mastcam image. Raster location #1 hit a small fragment of freshly dislodged

257   material from Mojave. (Additional 3 msec "dark" passive measurements were acquired on the

258   ultimate drill hole tailings on Sol 883. However, the relatively thin tailings pile was partially

259   removed by the LIBS laser blasts and the associated passive data are not used here.) CheMin

260   results from the nearby full drill analysis showed the sample to contain plagioclase (28 wt%),

261   augite (2 wt%), pigeonite (7 wt%), magnetite (4 wt%), hematite (3 wt%), jarosite (4 wt%),

262   apatite (3 wt%), phyllosilicate (6 wt%), trace (~1 wt %) ilmenite and quartz, and 42 wt%

263   amorphous materials (cf. Rampe et al. 2015a,b).

264   **Telegraph Peak**. Figure 7 shows a RMI mosaic and locations of a 5x1 raster on the full drill

265   hole at Telegraph Peak acquired on Sol 910 along with the Mastcam image. CheMin results

266   from a nearby full drill analysis showed the sample to contain plagioclase (30 wt%), potassium

267   feldspar (5 wt%), orthopyroxene (4 wt%), pigeonite (5 wt%), magnetite (9 wt%), cristobalite (7

268   wt%), jarosite (2 wt%), apatite (3 wt%), no phyllosilicates, augite, and trace (~1 wt %) olivine,

269   hematite, ilmenite and quartz, , with 31 wt% amorphous materials (cf. Rampe et al. 2015b).

270   **Long Distance Observations.**

271   The relatively low atmospheric opacity ($\tau < 0.65$) that occurred during Sols 432-492 (L_s

272   40-67°) was exploited to test the long-range capability of ChemCam passive spectra by acquiring

273   observations on targets up to 8 km from the rover (Table 1). These included portions of the

274   Bagnold Dune region south of the rover, the Hematite Ridge (HR) area, a "fan" region south of

275   Hematite Ridge (referred to by Grotzinger et al. (2015b) as part of a "draping strata" unit) and

276   underlying light-toned materials (Fig. 1a). As an example of these data sets, Figure 8 shows a

277   Mastcam false-color image with outlines designating the locations of two RMI mosaics

278   associated with ChemCam passive 1x10 rasters acquired on Sol 467 (described further below).

279   Light-toned mounds at the base of the "fan" materials were observed on Sol 492 along with the

280   top of Hematite Ridge, as shown in Figure 9.

281   **RESULTS**

282   **Overview of spectral features and parameters**

283   Representative spectra from the samples are displayed in Figure 10. The Windjana drill

284   tailings exhibit the lowest relative reflectance and a relatively flat spectrum, consistent with the

285   magnetite detected by CheMin. By comparison, the Confidence Hills spectrum (Stovepipe Wells

286   target) shows a deep ~535 nm absorption band and a near-infrared falloff that occurs near 785

287   nm, consistent with the hematite detected by CheMin (Table 2). A weak 433 nm absorption

288   band is consistent with the presence of minor jarosite as well. The presence of the 433 nm band

289   is somewhat more distinct in the Bonanza King spectrum, which is otherwise one of the flattest

290   spectra observed by ChemCam. The lack of appreciable slopes in this spectrum suggests a

291   relatively large amount of a spectrally neutral material such as magnetite. For comparison,

292   Telegraph Peak shows a similarly flat spectrum and was found by CheMin to contain ~10 wt%

293   magnetite. The minor 433 nm band in Telegraph Peak is also consistent with the 2 wt% jarosite

294   detected by CheMin, and suggests that a similar amount is likely present in Bonanza King. The

295   Perdido2 broken fragment demonstrates the deepest 433 nm band yet observed by ChemCam,

296   along with one of the deepest near-infrared falloffs, beginning near 700 nm. These features are

297   consistent with significant jarosite at this location, as demonstrated in more detail below.

298   The Mojave spectrum has a slightly shallower ~535 nm band than the Stovepipe Wells

299   target on Confidence Hills (and correspondingly lower hematite content from CheMin). Mojave

300   has twice the weight percent of jarosite than Telegraph Peak according to CheMin results, and its

301   433 nm band is correspondingly deeper. However, the Stovepipe Wells spectrum exhibits a 433

14

302   nm band of intermediate depth, despite it having the lowest jarosite content among these three

303   sites (Table 3). Furthermore, even the jarosite-free Cumberland sample's spectrum suggests a

304   nearly equivalent calculated 433 nm band depth, and the low reflectance Windjana spectrum's

305   433 nm band depth is even larger. These "false-positives" may result from additional noise in

306   this spectral region arising from the shorter exposure (3 msec) used for these two locations

307   compared to the other two samples (Table 3). It also illuminates the difficulty in linearly

308   correlating spectral band depths with abundance in the visible region of the spectrum,

309   particularly when opaque phases such as magnetite are present.

310   Figure 11 compares some of the key visible and near-infrared spectral parameters among

311   the drill tailing spectra (including spectra from additional raster locations from the sequences

312   listed in Table 1). The Confidence Hills spectrum (Stovepipe Wells) exhibits the largest 535 nm

313   band depth and most negative 600 nm band depth (consistent with the presence of hematite),

314   whereas the less oxidized Cumberland tailings exhibit the lowest 535 nm band depths (Fig. 11a).

315   The flat spectra of Bonanza King and Telegraph Peak result in their low 670/440 nm ratios and

316   high 600 nm band depths (Figs. 11a-b). Comparison of the 600/840 nm ratio and slopes (Fig.

317   11c) reveals a continuum of values ranging from low ratios and high slopes in the more oxidized

318   Confidence Hills sample to the high ratios and low slopes associated with less oxidized Bonanza

319   King. The location of Windjana parameters slightly below this trend is likely related to slightly

320   greater shadowing of the surface related to the higher phase angle (Table 1, Fig. 2, cf. Johnson et

321   al. 2015). Finally, the 750 to 840 nm slopes are least negative for Windjana (Fig. 11d),

322   consistent with their low relative reflectance and moderately flat spectra.

323   **Comparison to laboratory spectra**

324   In Figure 12 laboratory spectra of jarosite, ferricopiapite, and natrojarosite are plotted

325   with the Perdido2 spectrum (multiplied by 3.25 for ease of comparison). These ferric sulfates

326   exhibit similar, relatively narrow absorption bands near 433 nm and a downturn at wavelengths

327   less than about 410 nm. They also show pronounced downturns in reflectance at wavelengths

328   greater than about 700 nm. The ~433 nm feature has been observed in laboratory and terrestrial

329   field work but never on Mars (e.g., Cloutis et al. 2006a; McCollom et al. 2014, Sobron et al.

330   2014; Sklute et al. 2015). McCollom et al. (2014) demonstrated that this feature is more

331   apparent at low Fe# (= $100 \times$ Fe/(Al+Fe) on a molar basis). Figure 12 shows two of their

332   natrojarosite spectra with Fe# values of 10 and 20. The ChemCam LIBS spectra acquired on Sol

333   725 of the nearby Perdido target (the block directly above raster location #5 in Figure 4) reveal

334   average contents for Fe (19.9 wt %) and Al (11.1 wt %), which corresponds to an intermediate

335   Fe# (~46). Although it is unlikely that each LIBS location sampled only pure ferric sulfate, this

336   intermediate Fe# may be one reason that the 433 nm band depth of Perdido2 (0.071; Table 3) is

337   less than that for the lab spectra in Figure 12 (e.g., 0.310 for the jarosite spectrum).

338   Figure 13 shows laboratory spectra of ferric oxides compared to the Confidence Hills

339   (Stovepipe Wells) and Mojave spectra (contrast-enhanced to facilitate comparisons). Although

340   spectral features in the ChemCam spectra are subtle, the absorption near 535 nm and the flat

341   region near 660 nm are distinct from typical passive spectra. Combined with the minor spectral

342   downturn > 750 nm, these features are all consistent with a combination of crystalline and/or

343   nanophase hematite. Contributions from other crystalline or poorly crystalline hydroxylated

344   Fe(III) oxides (e.g., maghemite, ferrihydrite, and magnetite) or sulfates (e.g., schwertmannite)

345   cannot be excluded and may be indicated by the small shifts in spectral maxima and minima

346   relative to the hematite endmember. Nonetheless, for those iron oxides deemed above the

347   detection limits CheMin reported ~4 wt% magnetite and 3 wt% hematite in Mojave and 4 wt%

348   magnetite and 8 wt % hematite in Confidence Hills (Table 2; Cavanagh et al. 2015; Rampe et al.

349   2015b).

350   **Long-distance spectra**

351   Two examples from the long distance experiments are presented in Figure 14. The HR1

352   region (Fig. 14a) included targets in the near field (locations #1-3) consistent with typical dusty

353   martian areas. Locations #4, 5, and 8 fell on predominantly dark dune materials and exhibited

354   the lowest relative reflectance spectra, with gradual downturns at wavelengths greater than about

355   750 nm, consistent with mafic materials (olivine, pyroxene) in the dune sands. However,

356   locations on Hematite Ridge (#6, 7, 9, and 10) exhibited flatter spectra in the ~660 nm region, a

357   perceptibly deeper ~535 nm band, and a steeper downturn > 750 nm. As with the Confidence

358   Hills spectra, these features are also consistent with small amounts of crystalline hematite

359   associated with Hematite Ridge and similar nearby materials. Similar results were found for the

360   HR2 region, where dune materials in locations #4, 5, and 8 exhibited spectra distinct from the

361   locations on Hematite Ridge (#6 and 10), particularly in the near-infrared, again consistent with

362   hematite (Fig. 14b).

363   Figure 15 shows the results of targeting the light-toned mounds that occur near the base

364   of the "fan" materials to the south of Hematite Ridge. In this raster, the hematite-bearing regions

365   correspond to locations #3, 4 and 5 and exhibited the same features described above. The dune

366   materials were sampled by locations #7, 8, and 9, whereas the "fan" material is represented by

367   location #10 and exhibited a similar spectral shape to the dunes but a higher relative reflectance.

368   This may result from a slightly smaller grain size of the materials comprising the "fan" and/or a

369   photometric effect. Location #6 sampled the light-toned mound itself, but other than a distinctly

17

370 high relative reflectance there are no diagnostic spectral features other than the typical ferric

371 absorption edge associated with martian dust. This could be consistent with the presence of

372 phyllosilicate-bearing and/or sulfate minerals, given their typically neutral spectra in this

373 wavelength region.

374   The results of all long-distance observations (Table 1) are summarized in Figure 16 by

375 comparing spectral parameters similar to those used in Figure 11 as well as the 750 nm inflection

376 (band depth). For each data set in Figure 16 the raster location numbers are shown next to each

377 symbol. Based on comparing spectral features and their locations in RMI images, outlines were

378 drawn around distinctive spectral parameter regions associated with five unit types: dunes, "fan"

379 materials, typical dusty foreground regions, hematite-like areas, and the light-toned mound. The

380 typical dusty foreground areas exhibit nearly flat 750 nm to 840 nm slopes, large 670 nm to 440

381 nm (red-blue) slopes, and among the smallest 750 nm band depths. By comparison, the dune

382 materials exhibit small 535 nm band depths, more negative near-infrared slopes, and the lowest

383 red-blue slopes. The "fan" materials fall within the spectral parameter space of the dunes, but at

384 relatively low 535 nm and 750 nm band depths and high 670 nm to 440 nm slopes. The light-

385 toned mound areas are relatively distinct with their large red-blue slopes. The hematite-like

386 materials exhibit the largest 535 nm band depths and most negative near-infrared slopes and 750

387 nm band depths, with relatively high red-blue slopes.

DISCUSSION

389   ChemCam passive spectra provide a complementary perspective on the occurrence of

390 iron-bearing minerals in drill tailings, freshly disturbed surfaces, and relatively dust-free areas

391 that is consistent with results from other instruments. As a reconnaissance tool to investigate

392 areas worthy of detailed in situ investigations, these unique data add value to other remote

18

393   sensing observations that use LIBS spectra and Mastcam multispectral data (Jackson et al., 2015;

394   Wellington et al. 2015, this issue). Among the spectra investigated here, hematite-bearing

395   materials are evident in the Confidence Hills and Mojave materials, consistent with CheMin

396   results (Table 2). Hematite-bearing spectra were also observed in multiple long-distance

397   observations near and on materials associated with Hematite Ridge, consistent with CRISM

398   orbital observations (Milliken et al. 2010; Fraeman et al. 2013, 2015). Similarly, observations of

399   the dark dune materials south of the rover exhibited long-distance spectra indicative of the

400   presence of olivines and/or pyroxenes, consistent with CRISM observations (Seelos et al. 2014;

401   Ehlmann and Buz, 2015; Lapotre et al. 2015).

402   The low reflectance, spectrally flat nature of magnetite has a nonlinear contribution to

403   spectra in the visible wavelength region (Cloutis et al. 2011), and was considered a viable

404   candidate for the Windjana and Telegraph Peak drill tailings prior to their sample analyses. The

405   9-12 wt% magnetite abundances determined for both samples by CheMin (Table 2) were

406   consistent with these predictions. The similarity between Telegraph Peak and Bonanza King

407   spectra (Fig. 10) suggests that the latter has a similar contribution from magnetite (or other

408   minerals with dark, neutral spectra such as ilmenite). Moreover, the ~3-4 wt% magnetite

409   abundance determined by CheMin in the other drill samples (Table 2) provided a darkening

410   agent in those samples that contributed to relative reflectance values that are moderate for Mars

411   (typically below 0.25).

412   The presence of a 433 nm absorption band agrees with the CheMin detection of jarosite

413   in the Mojave, Telegraph Peak, and Confidence Hills drill tailings (Table 2). We interpret the

414   combination of a deep 433 nm band in the Perdido2 target spectrum and the strong decrease in

415   relative reflectance at wavelengths > 700 nm to represent a significant contribution from ferric

416   sulfate in that target, for which CheMin mineralogy data were not acquired. Because calculation

417   of 433 nm band depths was subject to band-to-band noise in the ChemCam VIO detector,

418   attempts to correlate band depth with ferric sulfate abundance were inconsistent, even when

419   averaging over 5 nm intervals (Table 3). Nonetheless, comparison of spectra shown in Figure 10

420   suggests that ferric sulfates such as jarosite are a likely component of the Bonanza King

421   materials as well. This emphasizes how the iterative interpretations of ChemCam passive spectra

422   with CheMin mineralogy can be used to expand interpretations of remotely-sensed observations

423   and enhance the predictive capability of such reconnaissance observations. Adding observations

424   from other payload elements such as Mastcam multispectral imaging and ChemCam and APXS

425   elemental chemistry can also assist with interpretations of detailed variations, as explored by

426   Wellington et al. (2015) and Jackson et al. (2015).

427   At the Pahrump Hills locality, Confidence Hills is the stratigraphically lowest drilled

428   sample, at the bottom of the Pahrump Member of the Murray Formation, followed by Mojave

429   and Telegraph Peak near the top (Stack et al., 2015; Grotzinger et al. 2015b). The decrease in

430   hematite and increase in magnetite concentrations from Confidence Hills to Telegraph Peak

431   suggests that reducing conditions were more prevalent higher in the sequence. The additional

432   presence of ferric sulfates such as jarosite suggests a relatively acidic environment, at least

433   during some (perhaps limited) time in the past. In situ diagenetic processes likely occurred with

434   variable pulses of iron-bearing fluids and associated oxidation, possibly aided by leaching of

435   sedimentary rocks via hydrothermal processes. There also could have been a combination of

436   relatively pristine components mixed with a different source that was more chemically weathered

437   (McClennan et al. 2015). In terrestrial settings, changes in the redox state can occur without

438   significant changes to the bulk chemistry of the constituent materials, and can occur erratically

439   over short spatial distances (as observed in some of the mm-scale observations investigated

440   here). Tracking the occurrence of these minerals throughout the rover traverse is therefore an

441   important part of understanding the geochemical and spatial evolution of materials near the base

442   of Mt. Sharp.

443   IMPLICATIONS

444   The methods developed by Johnson et al. (2015) to use the ChemCam instrument as a

445   passive reflectance spectrometer afford the opportunity to enhance the science return from the

446   Curiosity rover by providing additional constraints and spatial sampling of the mineral diversity

447   along the rover's traverse. Although variable surface dust subdues many spectral features in the

448   400-840 nm wavelength region, drill tailings, freshly disturbed materials, and relatively dust-free

449   (e.g., wind-abraded) samples provide the opportunity to investigate with greater spectral contrast

450   the band positions, shapes, depths and spectral slopes of passively collected ChemCam spectra.

451   The ChemCam relative reflectance spectra presented here include the first documented evidence

452   for the presence of an absorption band near 433 nm in spectra of in situ martian materials.

453   Combined with a spectral downturn longward of 700 nm, these spectra are consistent with

454   detections of a ferric sulfate such as jarosite (e.g., Cloutis et al. 2006a; McCollom et al.; 2014,

455   Sobron et al. 2014; Sklute et al. 2015). Additionally, enrichments in ferric oxides such as

456   hematite have been identified in select drill tailings as well as in landscape-scale features higher

457   on Mt. Sharp.

458   Mineralogical constraints from ChemCam passive spectra are important to daily

459   operations of the rover and targeting of potential in situ analysis locations, particularly when

460   combined with other remote sensing data sets. For example, this information can be used as an

461   additional means of deciphering the chemostratigraphy and mineralogy of rock facies observed

21

462   along the traverse (e.g., Vaniman et al. 2014; Anderson et al. 2015a; Fraeman et al. 2013;

463   Mangold et al. 2015), variations in igneous mineralogy (e.g., Stolper et al. 2013; Sautter et al.

464   2014; Schmidt et al. 2014), compositional and mineralogical variability related to grain size in

465   soils and rocks (e.g., Blake et al. 2013; Cousin et al. 2015), the effects of coatings (e.g., Lanza et

466   al. 2015), and geochemical observations and models of secondary mineral formation (e.g.,

467   McLennan et al. 2014; Blaney et al. 2014; Treiman et al. 2014; Bridges et al. 2015; Bristow et al.

468   2015). Long-distance observations are useful for strategic planning of possible traverse routes

469   and future targets (e.g., Vasavada et al. 2014; Fraeman et al. 2015).

470   Based on these results, ongoing rover in situ and long-distance observations of the lower

471   portions of Mt. Sharp will continue to reveal spectral variations attributable to variable

472   proportions of hematite, magnetite, ferric sulfates, iron-bearing clay minerals, and perhaps other

473   mixed occurrences of ferrous and ferric materials. Fresh materials (drill tailings, disturbed rocks)

474   will likely have the greatest potential to reveal spectral variations less contaminated by the

475   variable masking effects of dust coatings. Outcrops higher up on Mt. Sharp that exhibit spectral

476   and mineralogical variations visible to CRISM will also likely continue to prove fruitful targets

477   for ChemCam passive observations, helping guide the rover's path and contextualize other

478   science data. Investigations of the active and inactive portions of the barchan and longitudinal

479   dunes of the Bagnold dune field south of the rover should provide additional constraints on the

480   mineralogical variability of dune sands (Lapotre et al. 2015). The capability of the rover's

481   sampling system to generate and place on the surface two to three sieved, grain size separates

482   may provide the opportunity to investigate compositional variability as a function of grain size

483   within the sands.

22

484   Ongoing analyses of ChemCam passive spectra will continue to provide valuable

485   experience with rover-based visible/near-infrared point spectroscopy that will be valuable for the

486   upcoming Mars2020 mission. The SuperCam instrument selected as a payload element on that

487   rover will include combined LIBS, Raman, and visible/near-infrared (~400-900 nm) point

488   spectroscopy. In addition, the 1300-2600 nm region will be sampled by a separate spectrometer

489   where the light is dispersed sequentially by an acousto-optical tunable filter (Maurice et al. 2015;

490   Fouchet et al. 2015). Combined use of those techniques with multispectral imaging from the

491   Mastcam-Z payload element on Mars2020 (Bell et al. 2014) will provide compositional and

492   mineralogical reconnaissance information vital to selecting targets to sample, drill, and cache for

493   eventual sample return.

494

505

23

REFERENCES CITED

507 Anderson, R.B., and Bell, J.F. III (2010) Geologic mapping and characterization of Gale crater
508   and implications for its potential as a Mars Science Laboratory landing site. Mars, 5, 76–128.

509 Anderson, R., J.C. Bridges, A. Williams, L. Edgar, A. Ollila, J. Williams, M. Nachon, N.
510   Mangold, M. Fisk, J. Schieber, S. Gupta, G. Dromart, R. Wiens, S. Le Mouélic, O. Forni, N.
511   Lanza, A. Mezzacappa, V. Sautter, D. Blaney, B. Clark, S. Clegg, O. Gasnault, J. Lasue, R.
512   Léveillé, E. Lewin, K.W. Lewis, S. Maurice, H. Newsom, S.P. Schwenzer, and D. Vaniman
513   (2015a) ChemCam results from the Shaler outcrop in Gale Crater, Mars, Icarus, 249:2-21,
514   doi:10.1016/j.icarus.2014.07.025.

515 Anderson, R. C., Beegle, L., & Abbey, W. (2015b). Drilling on Mars: What We Have Learned
516   from the Mars Science Laboratory Powder Acquisition Drill System (PADS). In Lunar and
517   Planetary Science Conference, abstract# 2417.

518 Bell, J.F. III, H. Y. McSween, Jr., S.L. Murchie, J.R. Johnson, R. Reid, R.V. Morris, R.C.
519   Anderson, J.L. Bishop, N.T. Bridges, D.T. Britt, J.A. Crisp, T. Economou, A. Ghosh,
520   J.Greenwood, H.Gunnlaugsson, R.M. Hargraves, S. Hviid, J.M. Knudsen, M.B. Madsen, H.J.
521   Moore, R. Rieder, and L. Soderblom (2000) Mineralogic and compositional properties of
522   martian soil and dust: Preliminary results from Mars Pathfinder, Journal of Geophysical
523   Research, 105, 1721-1755.

524 Bell III, J.F., S.W. Squyres, R.E. Arvidson, H.M. Arneson, D. Bass, D. Blaney, N. Cabrol, W.
525   Calvin, J. Farmer, W.H. Farrand, W. Goetz, M. Golombek, J.A. Grant, R. Greeley, E.
526   Guinness, A.G. Hayes, M.Y.H. Hubbard, K.E. Herkenhoff, M.J. Johnson, J.R. Johnson, J.
527   Joseph, K.M. Kinch, M.T. Lemmon, R. Li, M.B. Madsen, J.N. Maki, M. Malin, E.
528   McCartney, S. McLennan, H.Y. McSween, Jr., D.W. Ming, J.E. Moersch, R.V. Morris, E.Z.
529   Noe Dobrea, T.J. Parker, J. Proton, J.W. Rice, Jr., F. Seelos, J. Soderblom, L.A. Soderblom,
530   J.N. Sohl-Dickstein, R.J. Sullivan, M.J. Wolff, and A. Wang (2004a) Pancam multispectral
531   imaging results from the Spirit rover at Gusev crater, *Science, 305,* 800-806.

532 Bell III, J.F., S.W. Squyres, R.E. Arvidson, H.M. Arneson, D. Bass, W. Calvin, W.H. Farrand,
533   W. Goetz, M. Golombek, R. Greeley, J. Grotzinger, E. Guinness, A.G. Hayes, M.Y.H.
534   Hubbard, K.E. Herkenhoff, M.J. Johnson, J.R. Johnson, J. Joseph, K.M. Kinch, M.T.
535   Lemmon, R. Li, M.B. Madsen, J.N. Maki, M. Malin, E. McCartney, S. McLennan, H.Y.
536   McSween, Jr., D.W. Ming, R.V. Morris, E.Z. Noe Dobrea, T.J. Parker, J. Proton, J.W. Rice,
537   Jr., F. Seelos, J. Soderblom, L.A. Soderblom, J.N. Sohl-Dickstein, R.J. Sullivan, C. Weitz,
538   M.J. Wolff (2004b) Pancam multispectral imaging results from the Opportunity rover at
539   Meridiani Planum, *Science, 306,* 1703-1709.

540   Bell III, J.F., et al. (2008) Visible to near-IR multispectral orbital observations of Mars, Ch. 8, in
541   The Martian Surface: Composition, Mineralogy, and Physical Properties, Cambridge
542   University Press, p. 169-192.

543   Bell, J.F. III, A. Godber, M.S. Rice, A.A. Fraeman, B.L. Ehlmann, W. Goetz, C.J. Hardgrove,
544   D.E. Harker, J.R. Johnson, K.M. Kinch, M.T. Lemmon, S McNair, S. Le Mouélic, M.B.
545   Madsen, and the MSL Science Team (2013) Initial Multispectral Imaging Results from the
546   Mars Science Laboratory Mastcam Investigation at the Gale Crater Field Site, Lunar and
547   Planetary Science Conference, 44, abstract #1417.

548   Bell J.F. III, J.N. Maki, G.L. Mehall, M.A. Ravine M.A. Caplinger, and the Mastcam-Z Science
549   Team (2014) Mastcam-Z: A Geologic, Stereoscopic,and Multispectral Investigation on the
550   NASA Mars-2020 Rover, Abstract #1151, Presented at "International Workshop on
551   Instrumentation for Planetary Missions (IPM-2014)," Greenbelt, Maryland, November 4-7.

552   Bish, D., D. Blake, D. Vaniman, P. Sarrazin, T. Bristow, C. Achilles, P. Dera, S. Chipera, J.
553   Crisp, R.T. Downs, J. Farmer, M. Gailhanou, D. Ming, J.M. Morookian, R. Morris, S.
554   Morrison, E. Rampe, A. Treiman, and A. Yen (2014) The first X-ray diffraction
555   measurements on Mars, IUCrJ, 1(6), doi:10.1107/S2052252514021150.

556   Bishop, J. L., & Murad, E. (1996). Schwertmannite on Mars? Spectroscopic analyses of
557   schwertmannite, its relationship to other ferric minerals, and its possible presence in the
558   surface material on Mars. Mineral Spectroscopy: A Tribute to Roger G. Burns, 5, 337-358.

559   Bishop, Janice L., Enver Murad, and M. Darby Dyar. "What Lurks in the Martian Rocks and
560   Soil? Investigations of Sulfates, Phosphates, and Perchlorates. Akaganéite and
561   schwertmannite: Spectral properties and geochemical implications of their possible presence
562   on Mars." American Mineralogist 100, no. 4 (2015): 738-746.

563   Blake, D.F., et al. Curiosity at Gale Crater, Mars: Characterization and analysis of the Rocknest
564   sand shadow (2013) Science, 341(6153):1239505, doi:10.1126/science.1239505.

565   Blaney, D. L., et al. (2014) Chemistry and texture of the rocks at Rocknest, Gale Crater:
566   Evidence for sedimentary origin and diagenetic alteration, Journal of Geophysical Research
567   Planets, 119, doi:10.1002/ 2013JE004590.

568   Bridges, J.C., S.P. Schwenzer, R. Leveille, F. Westall, R.C. Wiens, N. Mangold, T. Bristow, P.
569   Edwards, and G. Berger (2015) Diagenesis and clay mineral formation at Gale Crater, Mars,
570   Journal of Geophysical Research Planets, 120(1):1-19, doi:10.1002/2014JE004757.

571   Bristow, T.F., D.L. Bish, D.T. Vaniman, R.V. Morris, D.F. Blake, J.P. Grotzinger, E.B. Rampe,
572   J.A. Crisp, C.N. Achilles, D.W. Ming, B.L. Ehlmann, P.L. King, J.C. Bridges, J.L.
573   Eigenbrode, D.Y. Sumner, S.J. Chipera, J.M. Morookian, A.H. Treiman, S.M. Morrison, R.T.
574   Downs, J.D. Farmer, D. Des Marais, P. Sarrazin, M.M. Floyd, M.A. Mischna, and A.C.

575   McAdam (2015) The origin and implications of clay minerals from Yellowknife Bay, Gale
576   crater, Mars, American Mineralogist, 100(4):824-836, doi:10.2138/am-2015-5077.

577   Cavanagh, P.D. et al. (2015) Confidence Hills mineralogy and CheMin results from base of Mt.
578   Sharp, Pahrump Hills, Gale Craer, Mars, Lunar and Planetary Science Conference abstract
579   #2735.

580   Clark, R. N., et al (2003), USGS Digital Spectral Library splib05a, USGS Open File Report 03-
581   395.

582   Clegg, S. M., Wiens, R. C., Maurice, S., Gasnault, O., Sharma, S. K., Misra, A. K., ... &
583   Johnson, J. R. (2015). Remote Geochemical and Mineralogical Analysis with SuperCam for
584   the Mars 2020 Rover. In Lunar and Planetary Science Conference (abstract #2781).

585   Cloutis, E.A., et al. (2006a) Detection and discrimination of sulfate minerals using reflectance
586   spectroscopy, Icarus, 184, 121-157.

587   Cloutis, E.; Craig, M.; Kaletzke, L.; McCormack, K.; Stewart, L. (2006b) HOSERLab: A New
588   Planetary Spectrophotometer Facility, 37th Annual Lunar and Planetary Science Conference,
589   abstract no.2121.

590   Cloutis, E.S., M.A. Craig, R.V. Kruzeleck, W.R. Jamroz, A. Scott, F.C. Hawthorne, and S.A.
591   Mertzman (2008) Spectral reflectance properties of minerals exposed to simulated Mars
592   surface conditions, Icarus, 195, 140-169.

593   Cloutis, E.A., P. Hudon, T. Hiroi, M.J. Gaffey, and P. Mann (2011) Spectral reflectance
594   properties of carbonaceous chondrites: 2. CM chondrites. Icarus 216, 309-346.

595   Cousin, A., P.Y. Meslin, R.C. Wiens, W. Rapin, N. Mangold, C. Fabre, O. Gasnault, O. Forni, R.
596   Tokar, A. Ollila, S. Schröder, J. Lasue, S. Maurice, V. Sautter, H. Newsom, D. Vaniman, S.
597   Le Mouélic, D. Dyar, G. Berger, D. Blaney, M. Nachon, G. Dromart, N. Lanza, B. Clark, S.
598   Clegg, W. Goetz, J. Berger, B. Barraclough, D. Delapp, and MSL Science Team (2015)
599   Compositions of coarse and fine particles in martian soils at Gale: A window into the
600   production of soils, Icarus, 249:22-42, doi:10.1016/j.icarus.2014.04.052.

601   Dixon, E. M., A. S. Elwood Madden, E. M. Hausrath, and M. E. Elwood Madden (2015)
602   Assessing hydrodynamic effects on jarosite dissolution rates, reaction products, and
603   preservation on Mars, Journal of Geophysical Research Planets, 120, 625–642,
604   doi:10.1002,2014JE004779.

605   Downs, R.T. and the MSL Science Team (2015) Determining mineralogy on Mars with the
606   CheMin X-ray diffractometer, Elements, 11(1):45-50, doi:10.2113/gselements.11.1.45.

607   Ehlmann, B.L. and C.S. Edwards, (2014) Mineralogy of the martian surface, Annual Reviews of
608   Earth and Planetary Sciences, 42:291-315, doi:10.1146/annurev-earth-060313-055024.

26

609   Ehlmann, B.L. and J. Buz (2015) Mineralogy and fluvial history of the watersheds of Gale,
610   Knobel, and Sharp craters: A regional context for MSL Curiosity's exploration, Geophysical
611   Research Letters, 42(2):264-273, doi:10.1002/2014GL062553.

612   Farrand, W., J.F. Bell III, J.R. Johnson, S.W. Squyres, J. Soderblom, and D.W. Ming (2006)
613   Spectral variability in Visible and Near Infrared multispectral Pancam data collected at Gusev
614   Crater: Examinations using spectral mixture analysis and related techniques, Journal of
615   Geophysical Research, 111, E02S15, doi:10.1029/2005JE002495.

616   Farrand, W. H.; et al. (2007) Visible and near-infrared multispectral analysis of rocks at
617   Meridiani Planum, Mars, by the Mars Exploration Rover Opportunity, Journal of Geophysical
618   Research, 112, E06S02, 10.1029/2006JE002773.

619   Farrand, W. H., J. F. Bell, III, J. R. Johnson, R. E. Arvidson, L. S. Crumpler, J. A. Hurowitz, and
620   C. Schröder (2008a) Rock spectral classes observed by the Spirit Rover's Pancam on the
621   Gusev Crater Plains and in the Columbia Hills, Journal of Geophysical Research, 113,
622   E12S38, doi:10.1029/2008JE003237.

623   Farrand, W.H., J. F. Bell III, J. R. Johnson, J.L. Bishop, R. V. Morris (2008b) Multispectral
624   Imaging from Mars Pathfinder, Ch. 8, *in The Martian Surface: Composition, Mineralogy,*
625   *and Physical Properties*, Cambridge University Press.

626   Fouchet, T., Montmessin, F., Forni, O., Maurice, S., Wiens, R. C., Jonhson, J. R., ... &
627   SuperCam Team, T. (2015). The Infrared Investigation on the SuperCam Instrument for the
628   Mars2020 Rover. In Lunar and Planetary Science Conference abstract #1736.

629   Fraeman, A. A., Arvidson, R. E., Catalano, J. G., Grotzinger, J. P., Morris, R. V., Murchie, S. L.,
630   ... & Viviano, C. E. (2013) A hematite-bearing layer in Gale Crater, Mars: Mapping and
631   implications for past aqueous conditions. Geology, 41(10), 1103-1106.

632   Fraeman, A. A. C. S. Edwards, B. L. Ehlmann, R. E. Arvidson, J. R. Johnson, and M.S. Rice
633   (2015) Exploring Curiosity's Future Path From Orbit: The View Of Lower Mt. Sharp From
634   Integrated CRISM, HiRise, and THEMIS Datasets, Lunar and Planetary Science Conference,
635   abstract # 2124.

636   Grotzinger, J. P., & Milliken, R. E. (2012). The sedimentary rock record of Mars: Distribution,
637   origins, and global stratigraphy. In Sedimentary Geology of Mars (Vol. 102, pp. 1-48). SEPM
638   Special Publication, Tulsa, OK.

639   Grotzinger, J.P., et al. (2014) A habitable fluvio-lacustrine environment at Yellowknife Bay,
640   Gale Crater, Mars, Science, 343(6169), 1242777, doi:10.1126/science.1242777.

641 Grotzinger, J.P., J.A. Crisp, A.R. Vasavada, and the MSL Science Team (2015a) Curiosity's
642   mission of exploration at Gale Crater, Mars, Elements, 11(1):19-26,
643   doi:10.2113/gselements.11.1.19.

644 Grotzinger, J.P., et al. (2015b) Deposition,Exhumation, and Paleoclimate of an Ancient Lake
645   Deposit, Gale Crater, Mars (in review).

646 Jackson, R.S., R.C. Wiens, D.T. Vaniman, L. Beegle, O. Gasnault, H.E. Newsom, S. Maurice,
647   P.-Y. Meslin, S. Clegg, A. Cousin, S. Schröder, J.M. Williams (2015) ChemCam
648   Investigation of the John Klein and Cumberland Drill Holes and Tailings, submitted to Icarus.

649 Johnson, J.R. and Grundy, W.M. (2001) Visible/near-infrared spectra and two-layer modeling of
650   palagonite-coated basalts. Geophysical Research Letters, 28, 2101-2104.

651 Johnson, J.R., and 10 others (2001) Geological characterization of remote field sites using visible
652   and infrared spectroscopy: Results from the 1999 Marsokhod field test, Journal of
653   Geophysical Research, 106, 7683-7711.

654 Johnson, J.R., W.M. Grundy, and M.T. Lemmon, (2003) Dust deposition at the Mars Pathfinder
655   landing site: Observations and modeling of visible/near-infrared spectra, Icarus, 163, 330-
656   346.

657 Johnson, J. R., J. F. Bell, III, E. Cloutis, M. Staid, W. H. Farrand, T. McCoy, M. Rice, A. Wang,
658   and A. Yen (2007) Mineralogic constraints on sulfur-rich soils from Pancam spectra at Gusev
659   crater, Mars, Geophysical Research Letters, 34, L13202, doi:10.1029/2007GL02989.

660 Johnson, J.R., J.F. Bell III , S. Bender , D. Blaney , E. Cloutis , L. DeFlores , B. Ehlmann, O.
661   Gasnault , B. Gondet , K. Kinch , M. Lemmon, S. Le Mouélic , S. Maurice , M. Rice, R.
662   Wiens, MSL Science Team (2015) ChemCam Passive Reflectance Spectroscopy of Surface
663   Materials at the Curiosity Landing Site, Mars, Icarus, 249, 74–92.

664 Lanza, N.L., A.M. Ollila, A. Cousin, R.C. Wiens, S. Clegg, N. Mangold, N. Bridges, D. Cooper,
665   M. Schmidt, J. Berger, R. Arvidson, N. Melikechi, H. E. Newsom, R. Tokar, C. Hardgrove,
666   A. Mezzacappa, R.S. Jackson, B. Clark, O. Forni, S. Maurice, M. Nachon, R.B. Anderson, J.
667   Blank, M. Deans, D. Delapp, R. Léveillé, R. McInroy, R. Martinez, P.-Y. Meslin, and P. Pinet
668   (2015) Understanding the signature of rock coatings in laser-induced breakdown spectroscopy
669   data, Icarus, 249:62-73, doi:10.1016/j.icarus.2014.05.038.

670 Lapotre, M. G. A., Ehlmann, B. L., Ayoub, F., Minson, S. E., Bridges, N. T., Fraeman, A. A., ...
671   & Johnson, J. R. (2015). The Bagnold Dunes at Gale Crater---A Key to Reading the Geologic
672   Record of Mount Sharp. In Lunar and Planetary Science Conference abstract #1634.

673 Lemmon, M.T., et al. (2004) Atmospheric imaging results from the Mars Exploration Rovers:
674   Spirit and Opportunity, Science, 306, 1753-1756.

28

675 Mangold, N., et al. (2015) Chemical variations in Yellowknife Bay formation sedimentary rocks
676   analyzed by ChemCam on board the Curiosity rover on Mars, Journal of Geophysical
677   Research Planets, 120(3):452-482, doi:10.1002/2014JE004681.

678 Maurice, S., et al. (2012), The ChemCam instrument suite on the Mars Science Laboratory
679   (MSL) rover: Science objectives and mast unit description, Space Sci. Rev., 170, 95–166,
680   doi:10.1007/s11214-012-9912-2.

681 McLennan, S.M., et al. (2014) Elemental geochemistry of sedimentary rocks at Yellowknife
682   Bay, Gale Crater, Mars, Science, 343(6169), 1244734, doi:10.1126/science.1244734.

683 McLennan, S. M., Dehouck, E., Grotzinger, J. P., Hurowitz, J. A., Mangold, N., & Siebach, K.
684   (2015). Geochemical Record of Open-System Chemical Weathering at Gale Crater and
685   Implications for Paleoclimates on Mars. In Lunar and Planetary Science Conference, abstract
686   # 2533.

687 McCollom, Thomas M., Bethany L. Ehlmann, Alian Wang, Brian M. Hynek, and Thelma S.
688   Berquó [2014] Detection of iron substitution in natroalunite-natrojarosite solid solutions and
689   potential implications for Mars, American Mineralogist 99, no. 5-6, 948-964.

690 McSween, H.Y., Jr., S.L. Murchie, J.A. Crisp, N.T. Bridges, R.C. Anderson, J.F. Bell III, D.T.
691   Britt, J. Brückner, G. Dreibus, T. Economou, A. Ghosh, M.Golombek, J.Greenwood, J.R.
692   Johnson, H.J. Moore, R.V. Morris, T. J. Parker, R. Singer, and H. Wänke (1999) Chemical,
693   multispectral, and textural constraints on the composition and origin of rocks at the Mars
694   Pathfinder landing site, Journal of Geophysical Research, 104, 8679-8715.

695 Milliken, R. E., J. P. Grotzinger, and B. J. Thomson, Paleoclimate of Mars as captured by the
696   stratigraphic record in Gale Crater (2010) Geophysical Research Letters 37, 4, DOI:
697   10.1029/2009GL041870.

698 Milton, E.J., et al. (2009) Progress in field spectroscopy, Rem. Sens. Environ., 113, S92-S109.

699 Morris, R. V., H. V. Lauer Jr., C. A. Lawson, E. K. Gibson Jr., G. A. Nace, and C. Stewart
700   (1985), Spectral and other physicochemical properties of submicron powders of hematite (α-
701   Fe2O3), maghemite (γ-Fe2O3), magnetite (Fe3O4), goethite (α-FeOOH), and lepidocrocite
702   (γ-FeOOH), J. Geophys. Res., 90(B4), 3126–3144, doi:10.1029/JB090iB04p03126.

703 Morris, R.V., D.C. Golden, J.F. Bell III, (1997) Low-temperature reflectivity spectra of red
704   hematite and the color of Mars, Journal of Geophysical Research, 102, 912-9133.

705 Morris, R. V., et al. (2000), Mineralogy, composition, and alteration of Mars Pathfinder rocks
706   and soils: Evidence from multispectral, elemental, and magnetic data on terrestrial analogue,
707   SNC meteorite, and Pathfinder samples, J. Geophys. Res., 105, 1757–1817,
708   doi:10.1029/1999JE001059.

709 Nachon, M., Clegg, S. M., Mangold, N., Schröder, S., Kah, L. C., Dromart, G., ... & Wellington,
710   D., Calcium sulfate veins characterized by ChemCam/Curiosity at Gale Crater, Mars (2014)
711   Journal of Geophysical Research: Planets, 119, doi:10.1002/2013JE004588.

712 Pitman, K.M., et al. (2014) Reflectance spectroscopy and optical functions for hydrated Fe-
713   sulfates, American Mineralogist, 99, 1593-1603.

714 Rampe, E.B., et al. (2015a), Potential cement phases in sedimentary rocks drilled by Curiosity at
715   Gale Crater, Mars, Lunar and Planetary Science Conference 46, abstract #2038.

716 Rampe, E. B., Ming, D. W., Blake, D. F., Vaniman, D. T., Chipera, S. J., Bish, D. L., Bristow, T.
717   F., Morris, R. V., Achilles, C. N., Cavanagh, P. D., Downs, R. T., Dyar, M. D., Fairen, A. G.,
718   Farmer, J. D., Franz, H. B., Fendrich, K. V., Grotzinger, J. P., Morrison, S. M., Morookian, J.
719   M., Sarrazin, P., Sumner, D. Y., Treiman, A. H., and Yen, A. S. (2015b) Curiosity's Pahrump
720   Hills campaign in Gale crater, Mars: Mineralogy of the sediments and evidence for post-
721   depositional acid-sulfate alteration (in preparation).

722 Rice, M. S., Bell III, J. F., Godber, A., Wellington, D., Fraeman, A. A., Johnson, J. R., ... &
723   Grotzinger, J. P. (2013) Mastcam multispectral imaging results from the Mars Science
724   Laboratory investigation in Yellowknife Bay. In European Planetary Science Congress 2013,
725   id. EPSC2013-762 (Vol. 8, p. 762).

726 Roush, T.L., D.L. Blaney, and R.B. Singer (1993) The surface composition of Mars as inferred
727   from spectroscopic observations. In Remote Geochemical Analysis: Elemental and
728   Mineralogical Composition, ed. C.M. Pieters and P.A.J. Englert, New York: Cambridge
729   University Press, pp. 367-393.

730 Rossman, G.R. (1975)Spectroscopic and magnetic studies of ferric iron hydroxyl sulfates:
731   Intensification of color in ferric iron clusters bridged by a single hydroxide ion, Amer.
732   Mineral. 60, 698-704.

733 Sautter, V., C. Fabre, O. Forni, M.J. Toplis, A. Cousin, A.M. Ollila, P.Y. Meslin, S. Maurice,
734   R.C. Wiens, D. Baratoux, N. Mangold, S. Le Mouélic, O. Gasnault, G. Berger, J. Lasue, R.A.
735   Anderson, E. Lewin, M. Schmidt, D. Dyar, B.L. Ehlmann, J. Bridges, B. Clark, and P. Pinet,
736   Igneous mineralogy at Bradbury Rise: The first ChemCam campaign at Gale crater (2014)
737   Journal of Geophysical Research Planets, 119(1): 30-46, doi:10.1002/2013JE004472.

738 Schmidt, M. E., P. L. King, R. Gellert, B. Elliott, L. Thompson, J. A. Berger, J. Bridges et al.
739   Geochemical diversity and K-rich compositions found by the MSL APXS in Gale Crater,
740   Mars (2013), Mineralogical Magazine 77, no. 5, 2158.

741 Schmidt, M.E., J.L. Campbell, R. Gellert, G.M. Perrett, A.H. Treiman, D.L. Blaney, A. Ollila,
742   F.J. Calef III, L. Edgar, B.E. Elliott, J. Grotzinger, J. Hurowitz, P.L. King, M.E. Minitti, V.
743   Sautter, K. Stack, J.A. Berger, J.C. Bridges, B.L. Ehlmann, O. Forni, L.A. Leshin, K.W.

744   Lewis, S.M. McLennan, D.W. Ming, H. Newsom, I. Pradler, S.W. Squyres, E.M. Stolper, L.
745   Thompson, S. VanBommel, and R.C. Wiens (2014) Geochemical diversity in first rocks
746   examined by the Curiosity rover in Gale crater: Evidence for and significance of an alkali and
747   volatile-rich igneous source, Journal of Geophysical Research Planets, 119(1):64-81,
748   doi:10.1002/2013JE004481.

749   Seelos, K. D., Seelos, F. P., Viviano-Beck, C. E., Murchie, S. L., Arvidson, R. E., Ehlmann, B.
750   L., & Fraeman, A. A. (2014). Mineralogy of the MSL Curiosity landing site in Gale crater as
751   observed by MRO/CRISM. Geophysical Research Letters, 41(14), 4880-4887.

752   Sherman, D. M., R. G. Burns, and V. M. Burns (1982), Spectral characteristics of the iron oxides
753   with application to the Martian bright region mineralogy, J. Geophys. Res., 87(B12), 10169–
754   10180, doi:10.1029/JB087iB12p10169.

755   Singer, R.B., T. B. McCord, R. N. Clark, J.B. Adams, and R.L. Huguenin (1979) Mars surface
756   composition from reflectance spectroscopy: A summary, Journal of Geophysical Research,
757   84, 8415-8426.

758   Skulte, E.C., H.B. Jensen, A.D. Rogers, and R. J. Reeder (2015) Morphological, structural, and
759   spectral characteristics of amorphous iron sulfates, Journal of Geophysical Research Planets,
760   120, doi:10.1002/2014JE004784.

761   Sobron, P., J.L. Bishop, D.F. Blake, B. Chen, and F. Rull (2014), Natural Fe-bearing oxides and
762   sulfates from the Rio Tinto Mars analog site: Critical assessment of VNIR reflectance
763   spectroscopy, laser Raman spectroscopy, and XRD as mineral identification tools, Amer.
764   Mineral. 99, 1199-1205.

765   Stack, K. M., Grotzinger, J. P., Gupta, S., Kah, L. C., Lewis, K. W., McBride, M. J., ... & Yingst,
766   R. A. (2015). Sedimentology and Stratigraphy of the Pahrump Hills Outcrop, Lower Mount
767   Sharp, Gale Crater, Mars. In Lunar and Planetary Science Conference, abstract #1994.

768   Stolper, E.M., M.B. Baker, M.E. Newcombe, M.E. Schmidt, A.H. Treiman, A. Cousin, M.D.
769   Dyar, M.R. Fisk, R. Gellert, P.L. King, L. Leshin, S. Maurice, S.M. McLennan, M.E. Minitti,
770   G. Perrett, S. Rowland, V. Sautter, R.C. Wiens, and MSL Science Team (2013) The
771   petrochemistry of Jake_M: A martian mugearite, Science, 341 (6153):1239463,
772   doi:10.1126/science.1239463.

773   Thompson, L. et al. (2015) The composition of the Basal Murray Formation at Pahrump Hills,
774   Gale crater, Mars: implications for provenance and alteration history from an APXS
775   perspective, in preparation.

776   Treiman, A.H., R.V. Morris, D.G. Agresti, T.G. Graff, C.N. Achilles, E.B. Rampe, T.F. Bristow,
777   D.W. Ming, D.F. Blake, D.T. Vaniman, D.L. Bish, S.J. Chipera, S.M. Morrison, and R.T.

31

778   Downs (2014) Ferrian saponite from the Santa Monica Mountains (California, U.S.A., Earth):
779   Characterization as an analog for clay minerals on Mars with application to Yellowknife Bay
780   in Gale Crater, American Mineralogist, 99, doi:10.2138/am-2014-4763, 2234-2250.

781   Treiman, A.H. et al. (2015a) Mineralogy and genesis of the Windjana sandstone, Kimberley
782   area, Gale Crater, Mars, Lunar and Planetary Science Conference 46, abstract #2620.

783   Treiman, A.H. et al. (in preparation), Mineralogy and genesis of the Windjana sandstone,
784   (Kimberley area, Gale Crater, Mars) by CheMin X-ray diffraction: Sediment components, and
785   the nature of potassic rocks and sediments in Gale Crater, in preparation to Journal of
786   Geophysical Research, 2015b.

787   Vaniman, D.T., et al. (2014) Mineralogy of a mudstone at Yellowknife Bay, Gale Crater, Mars,
788   Science, 343(6169), 1243480, doi:10.1126/science.1243480.

789   Vasavada, A.R., J.P. Grotzinger, R.E. Arvidson, F.J. Calef, J.A. Crisp, S. Gupta, J. Hurowitz, N.
790   Mangold, S. Maurice, M.E. Schmidt, R.C. Wiens, R.M.E. Williams, and R.A. Yingst (2014)
791   Overview of the Mars Science Laboratory mission: Bradbury landing to Yellowknife Bay and
792   beyond, Journal of Geophysical Research Planets, 119(6):1134-1161,
793   doi:10.1002/2014JE004622.

794   Wellington, D., et al. (2014) Visible to Near-IR Spectral Units along the MSL Gale Crater
795   Traverse: Comparison of In Situ Mastcam and Orbital CRISM Observations, AGU Fall
796   Meeting, P43D-4015.

797   Wellington, D., J. Bell, J. Johnson, K. Kinch., M. Rice, A. Fraeman (this issue) Visible and
798   Near-Infrared Spectra of Select High-Interest Science Targets within Gale Crater Observed by
799   MSL Mastcam.

800   Wiens, R. and 80 others (2012) The ChemCam Instrument Suite on the Mars Science Laboratory
801   (MSL) Rover: Body Unit and Combined System Performance, Space Sci Rev., 170, 167-227.

802   Wiens, R. C., et al. (2013) Pre-flight calibration and initial data processing for the ChemCam
803   laser-induced breakdown spectroscopy instrument on the Mars Science Laboratory rover,
804   Spectrochimica Acta Part B: Atomic Spectroscopy 82, 1-27.

805   Wiens, R.C., S. Maurice, and the MSL Science Team (2015) ChemCam: Chemostratigraphy by
806   the first Mars microprobe, Elements, 11(1):33-38, doi:10.2113/gselements.11.1.33.

807   Williams, R.M.E., et al. (2013) Martian fluvial conglomerates at Gale Crater, Science,
808   340(6136):1068-1072, doi:10.1126/science.1237317.

809   Wray, J.J., (2013) Gale crater: The Mars Science Laboratory/Curiosity rover landing site,
810   International Journal of Astrobiology, 12(1):25-38, doi:10.1017/S1473550412000328.

811

Table 1. ChemCam observations used in this study.

Target	Sol	Sequence ID	Exposure time (msec)	LTST	Phase angle (deg)	τ_{880}[1]
Cumberland 2	289	2289	3	13:26	43	0.98
Windjana	619	2619	3	13:33	84	0.34
Perdido2	728	1728	30	11:41	22	0.76
Bonanza King	728	2728	30	11:48	27	0.76
Confidence Hills (Stovepipe Wells)	762	2762	3	13:06	41	0.88
Mojave_1	869	3869	30	12:04	49	0.92
Telegraph Peak	910	1910	30	10:29	58	0.80
Dunes	432	3432	30	11:27	80	0.64
Hematite Ridge 1	467	2466	30	12:00	68	0.44
Hematite Ridge 2	467	3466	30	12:15	68	0.44
Hematite Ridge 3	475	1475	30	12:51	70	0.45
Hematite Ridge 4	475	2475	30	13:07	72	0.45
Hematite Ridge 5	492	1492	30	11:20	64	0.46
Hematite Ridge 6	492	2492	30	11:35	65	0.46

[1]interpolated from preliminary atmospheric opacity measurements acquired at 880 nm

Table 2. Summary of CheMin results for drilled samples for minerals of interest.

Target	Jarosite (wt%)	Hematite (wt%)	Magnetite (wt%)
Cumberland 2	0	1	4
Windjana	<1?	1	12
Confidence Hills (Stovepipe Wells)	1.1	8.4	3.8
Mojave_2	3.5	3.1	3.5
Telegraph Peak	1.5	1.3	8.7

Table 3. 433 nm band depths of drill tailing spectra.

Target	Sol	Sequence ID	Raster location #	Exposure time (msec)	433 nm band depth
Cumberland 2	289	2289	1	3	0.023
Windjana	619	2619	1	3	0.047
Perdido2	728	1728	5	30	0.071
Bonanza King	728	2728	2	30	0.018
Confidence Hills (Stovepipe Wells)	762	2762	10	3	0.035
Mojave_1	869	3869	3	30	0.028
Telegraph Peak	910	1910	3	30	0.018

433 nm band depth computed using continuum calculated between 415 nm and 460 nm
wavelengths (±5 nm averaging used).

33

820
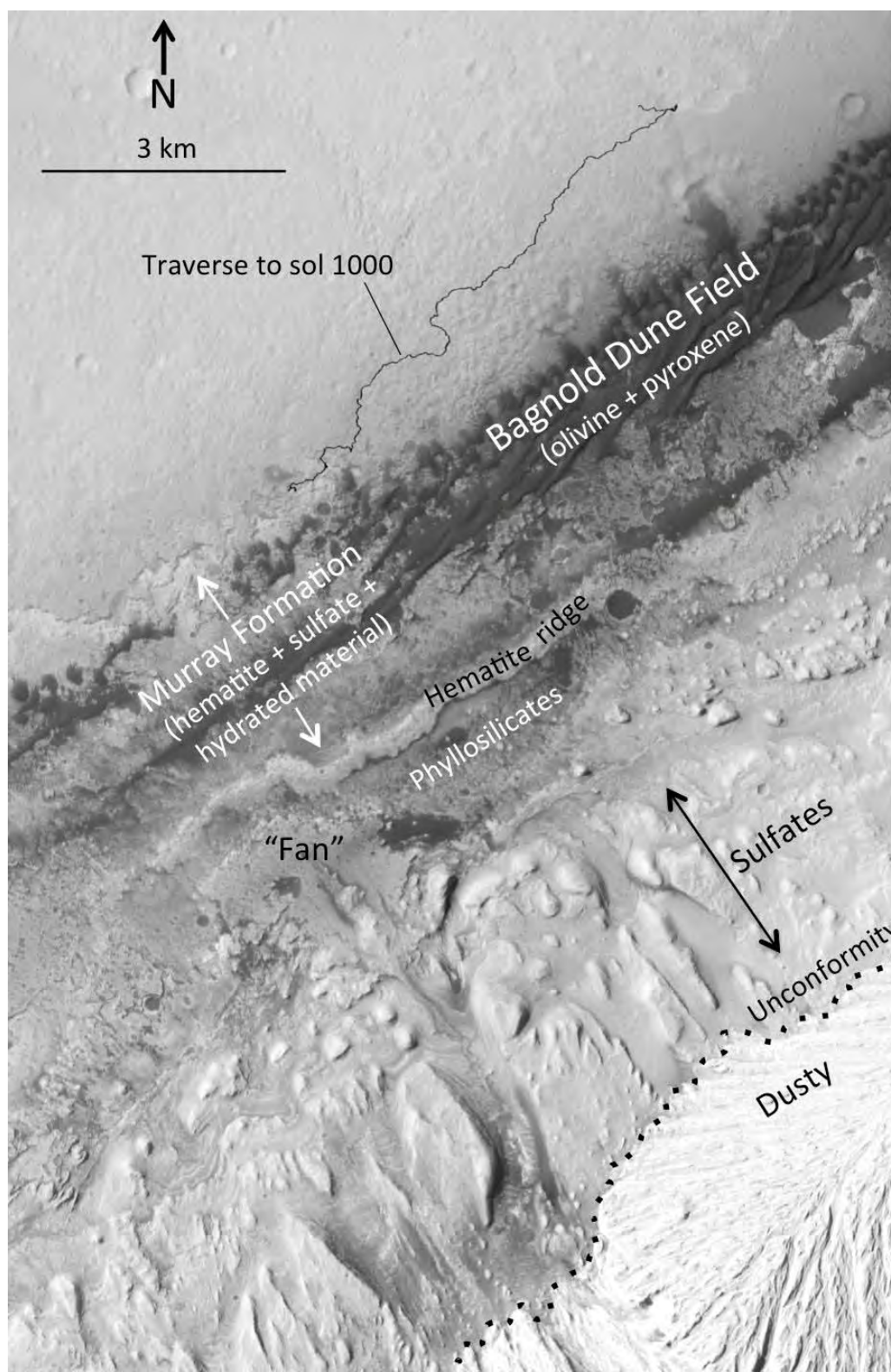
Figure 1a. Generalized orbital mineralogical map and Curiosity traverse path through Sol 1000
showing location of Hematite Ridge and nearby regions of interest. Based on mapping and data
from Milliken et al. (2010), Anderson and Bell (2010), and Fraeman et al. (2013).

34
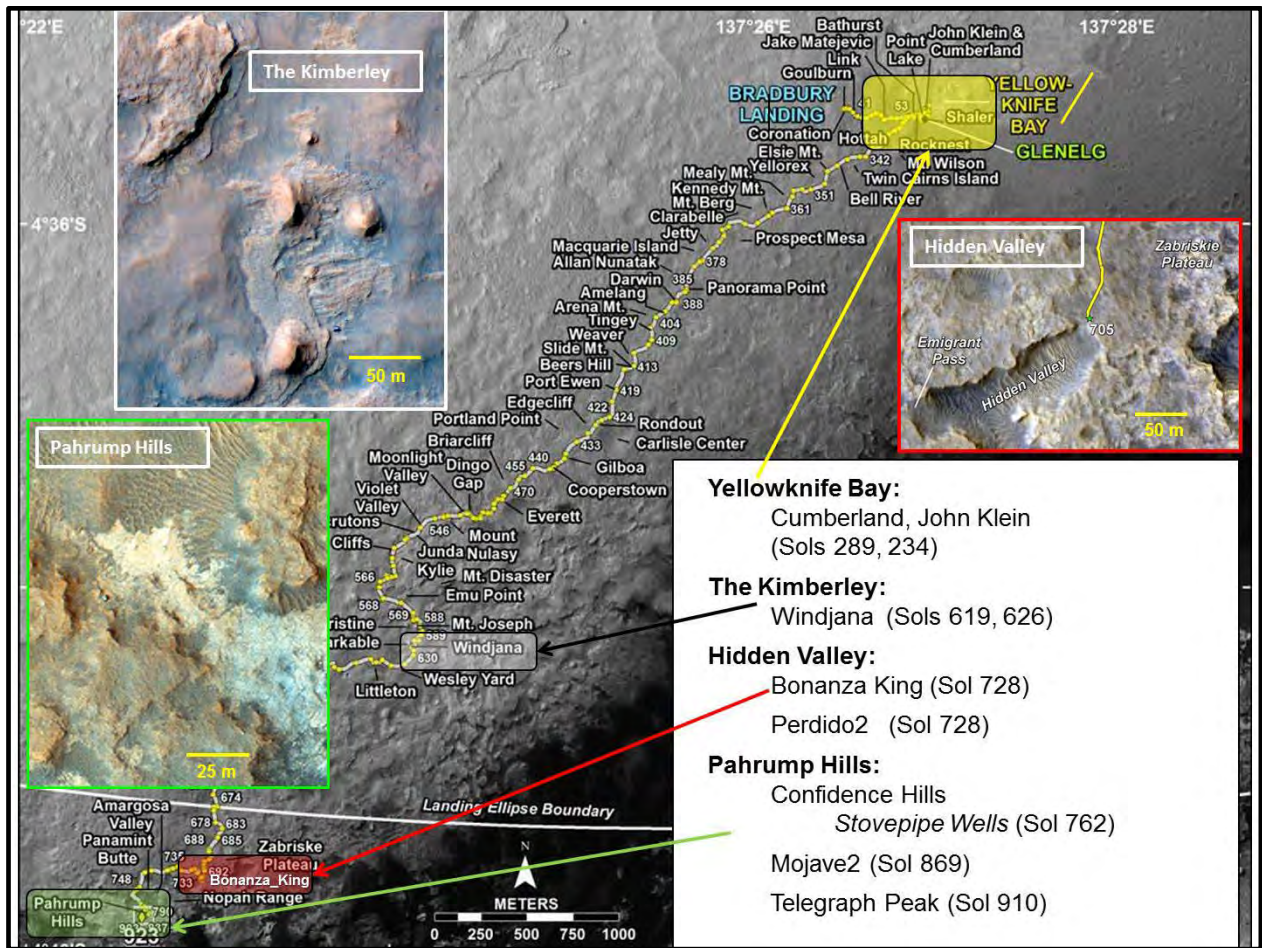
Figure 1b. Curiosity traverse map with areas of interest shown, along with inset false-color HiRISE images showing views of Hidden Valley, The Kimberley, and Pahrump Hills regions. (Base map from mars.nasa.gov/msl/multimedia/images/?ImageID=6993).

Figure 2. Sol 626 Mastcam M-34 image (0626ML0026760010302385E01) showing Windjana
mini-drill and full drill locations, along with Sol 619 RMI mosaic of mini-drill hole and tailings
(ccam02619; CR0_452446267, CR0_452447110) showing raster of eight locations.
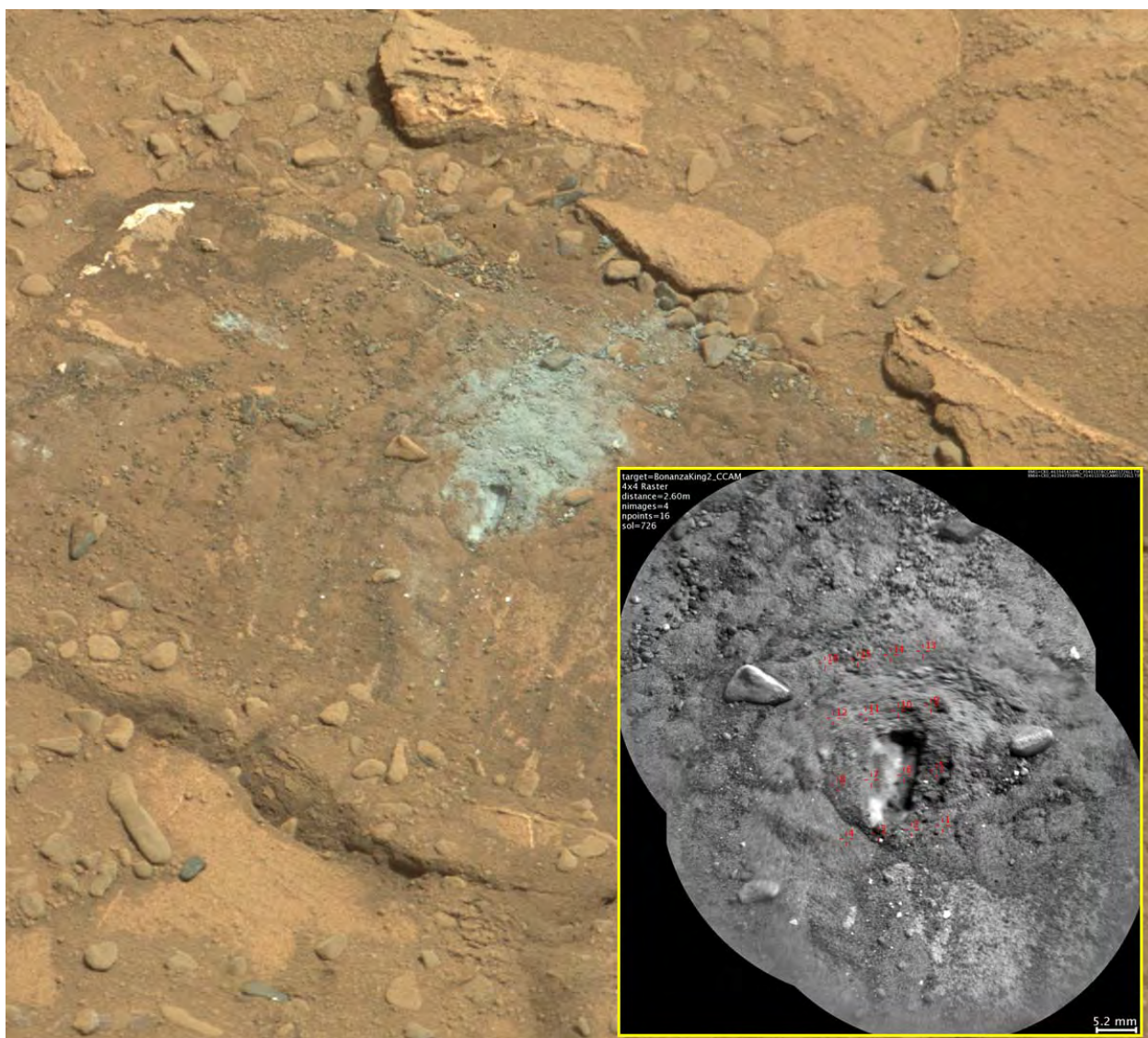
Figure 3. Portion of Sol 726 Mastcam M-100 image (0726MR0031010010402920E01) showing
Bonanza_King target after attempted mini-drill activities, along with Sol 726 RMI mosaic of
partial mini-drill area (ccam01726; CR0_461945420, CR0_461947398) and 4x4 ChemCam
raster locations.

37

837

Figure 4. Portion of Sol 725 Mastcam M-100 image (0725MR0030940000402844E01) showing Perdido2 target, along with Sol 728 RMI mosaic (ccam01728; CR0_462114621, CR0_462115029) showing 5x1 ChemCam passive raster locations. This was acquired after a ChemCam LIBS observation on Sol 725 (sequence 3725) on the broken rock Perdido (directly above this raster) exhibited passive spectra (3 msec "dark" exposures) with a potential 433 nm absorption band.

Figure 5. Sol 759 Mastcam M-100 image (0759MR0032680010403804E01) showing Stovepipe
Wells target (green box) and the Confidence Hills mini-drill and full drill holes, along with Sol
762 RMI mosaic (ccam02762; CR0_465137566, CR0_465138741) showing 10x1 ChemCam
raster locations on Stovepipe Wells (locations #4-10 occur on drill tailings).

39

849
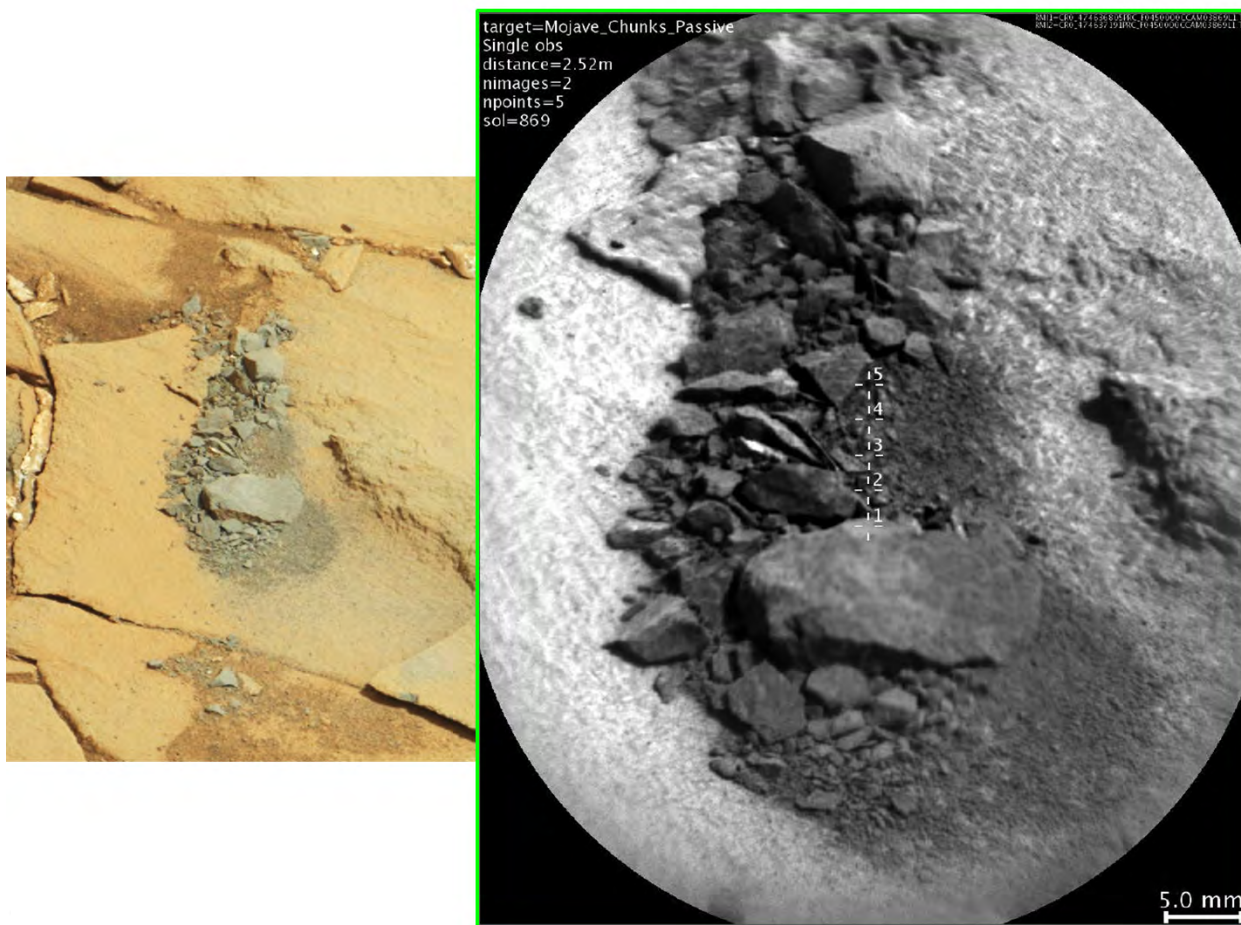
Figure 6. Portion of Sol 868 Mastcam M-100 image (0868MR0038120020501122E01) showing
fragments generated by mini-drill attempt on target Mojave_1, along with Sol 869 RMI mosaic
(ccam03869; CR0_474636805, CR0_474637191) showing 1x5 ChemCam passive raster
locations.

854
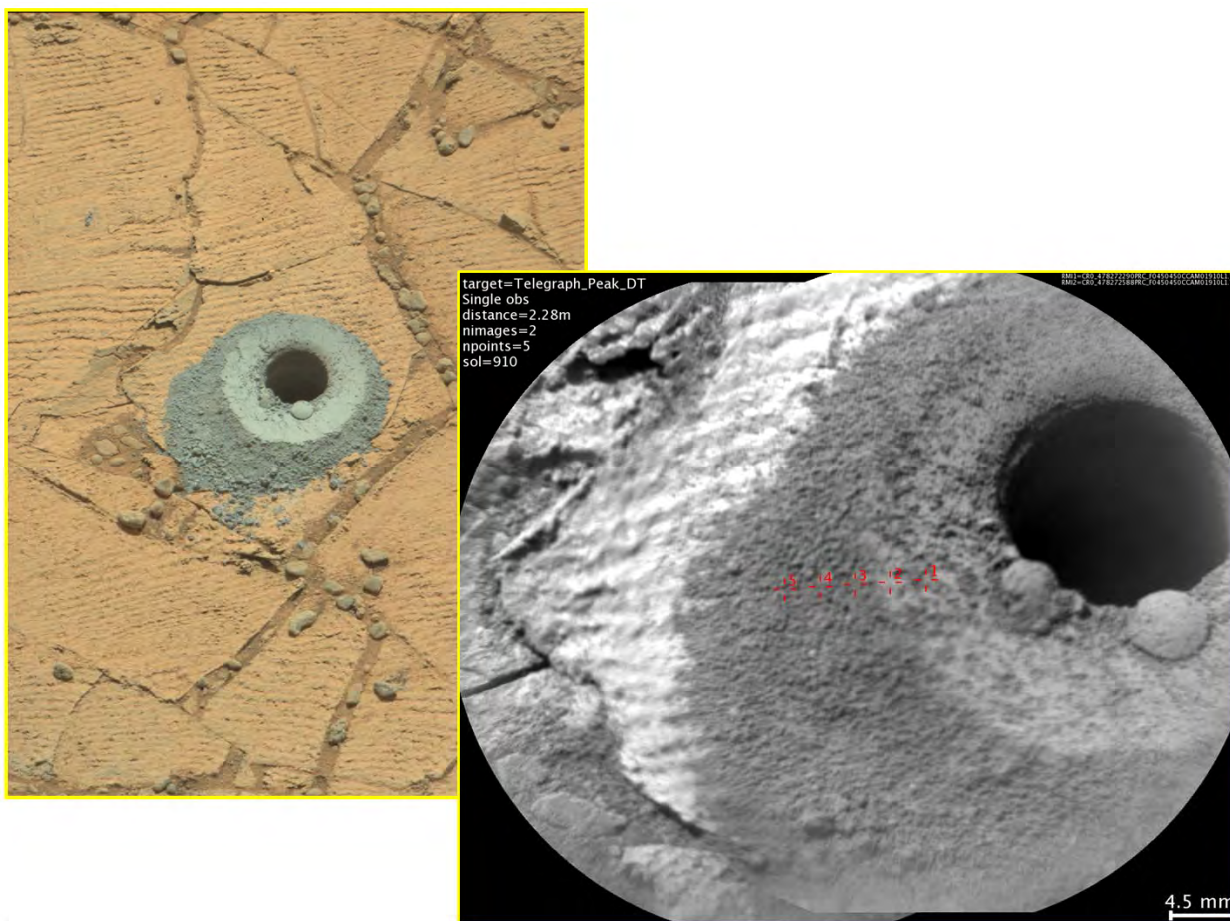
Figure 7. Portion of Sol 908 Mastcam M-100 image (0908MR0039720010501423E01) showing full drill hole on Telegraph Peak target, along with Sol 910 RMI mosaic (ccam01910; CR0_478272290, CR0_478272588) showing 5x1 ChemCam passive raster locations.
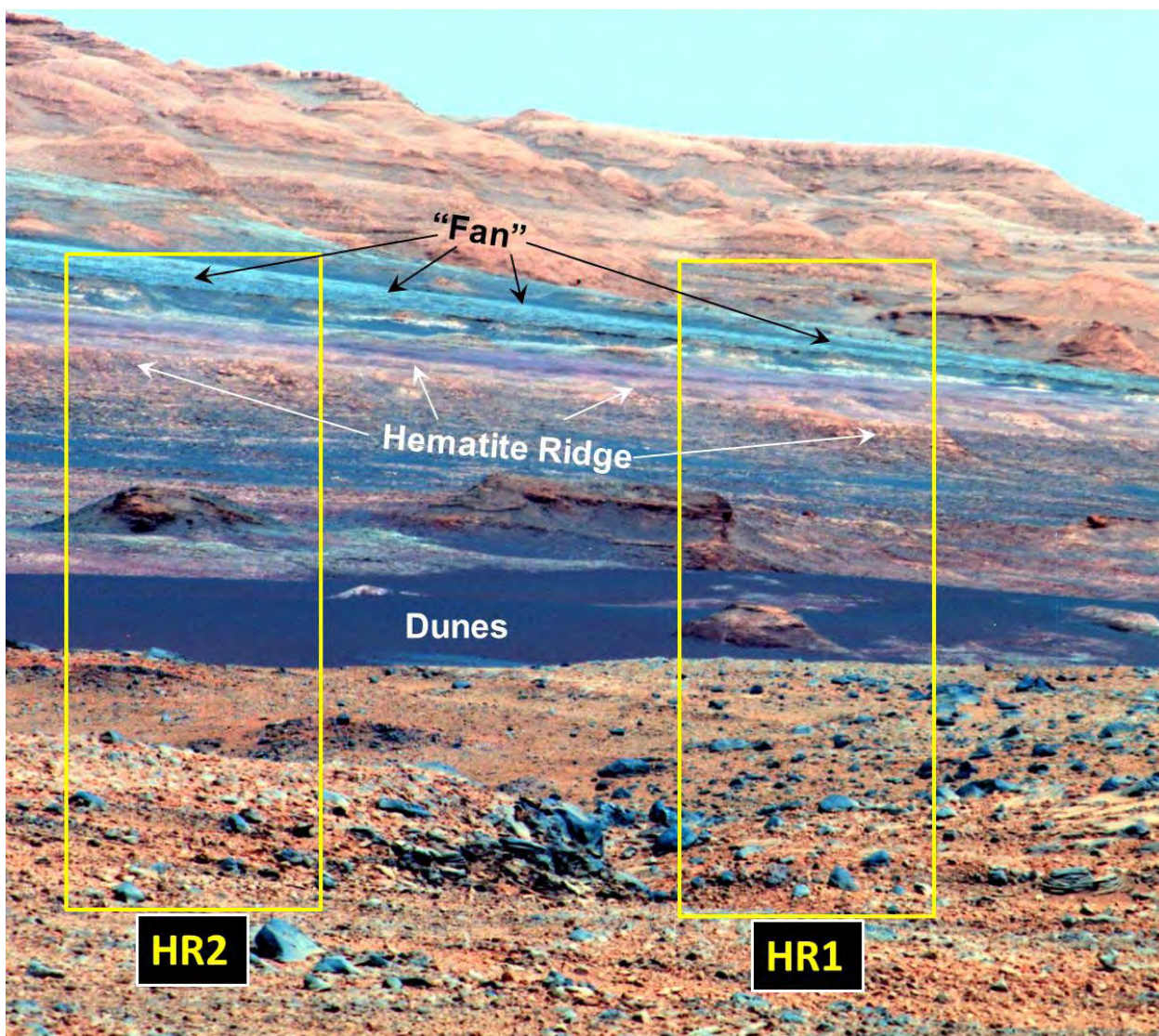
858

859   **Figure 8.** Portion of Sol 468 M-100 false-color image (sequence mcam01864; red = 805 nm,
860   green = 527 nm, blue = 447 nm) view toward 195° azimuth. Portion of Bagnold Dunes shown
861   along with Hematite Ridge promontory, and "fan" materials near base of Mt. Sharp (cf. Fig. 1a).
862   Superimposed are outlines of HR1 and HR2 RMI mosaics acquired on Sol 467 (Figure 14a-b).

863
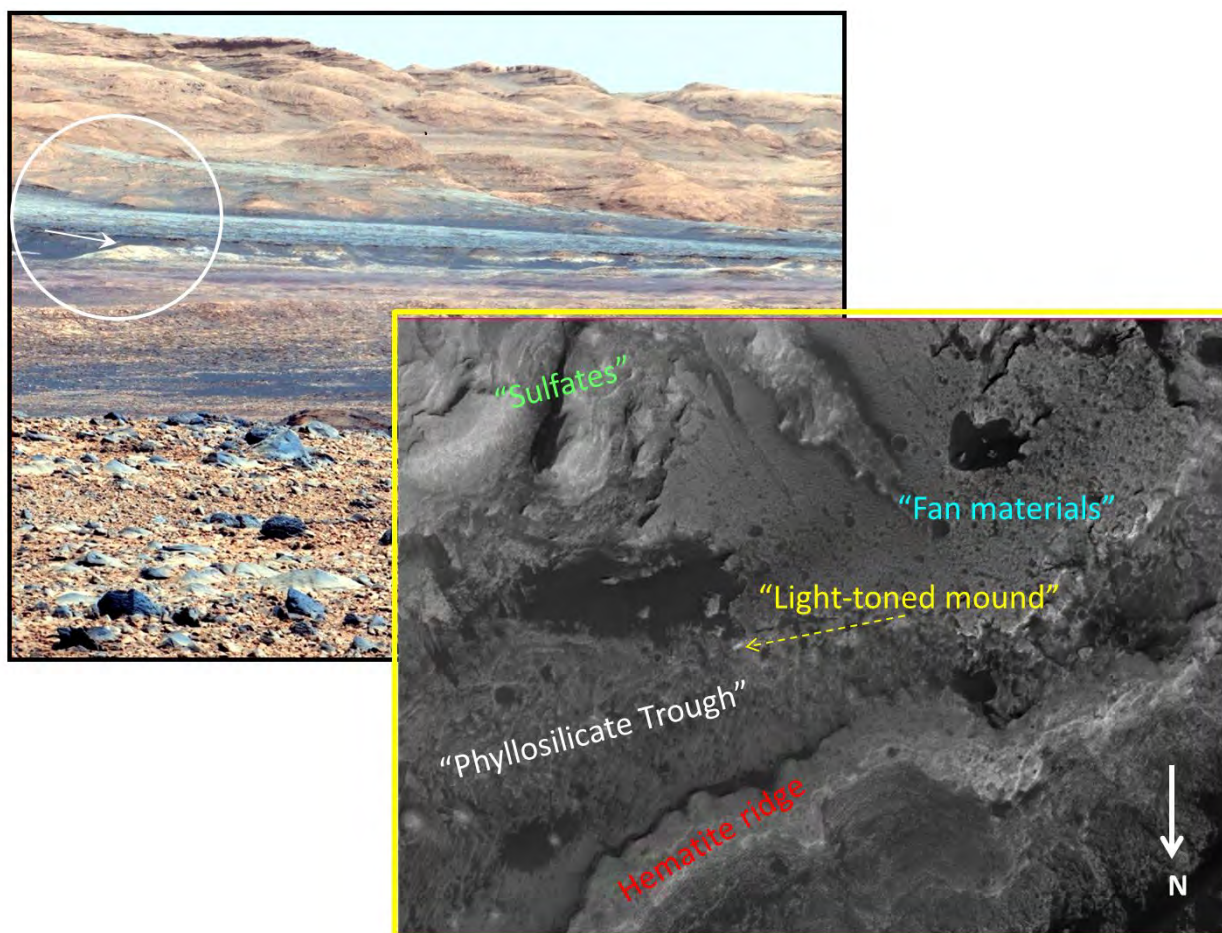
Figure 9. (*top*) Portion of Sol 475 Mastcam M-100 enhanced image
0475MR0018870000302889E01 (RGB=751, 527, 445 nm) showing light-toned mound (white
arrow within white circle) featured in Figure 15; (*bottom*); HiRISE image (with North at bottom
to facilitate comparison with rover's perspective looking south) labeled with general mapped
units (cf. Figure 1). "Light-toned mound" designated with yellow arrow is same shown in
Mastcam image. HiRISE scene is ~3 km across.

870
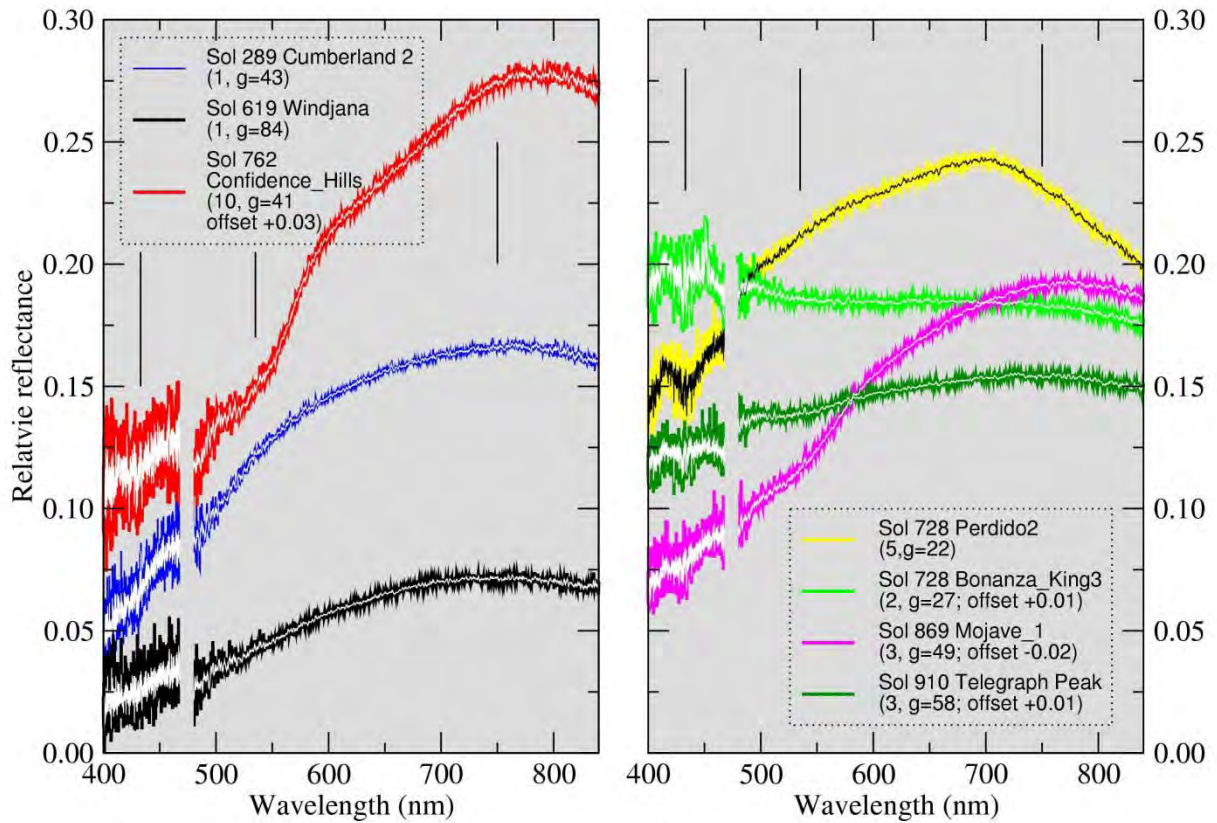
Figure 10. ChemCam relative reflectance spectra of representative locations for drill tailings
and fresh surfaces discussed here. Central white or black lines represent 5-channel average of
spectra shown in colors. Parenthetical notes refer to raster location number and phase angle of
observation (*g*). See Table 1 for details. Missing 468-480 nm data is region between ChemCam
detectors. Some spectra are offset for clarity, as shown in legend. Vertical bars correspond to
reference wavelength locations 433, 535, and 750 nm.
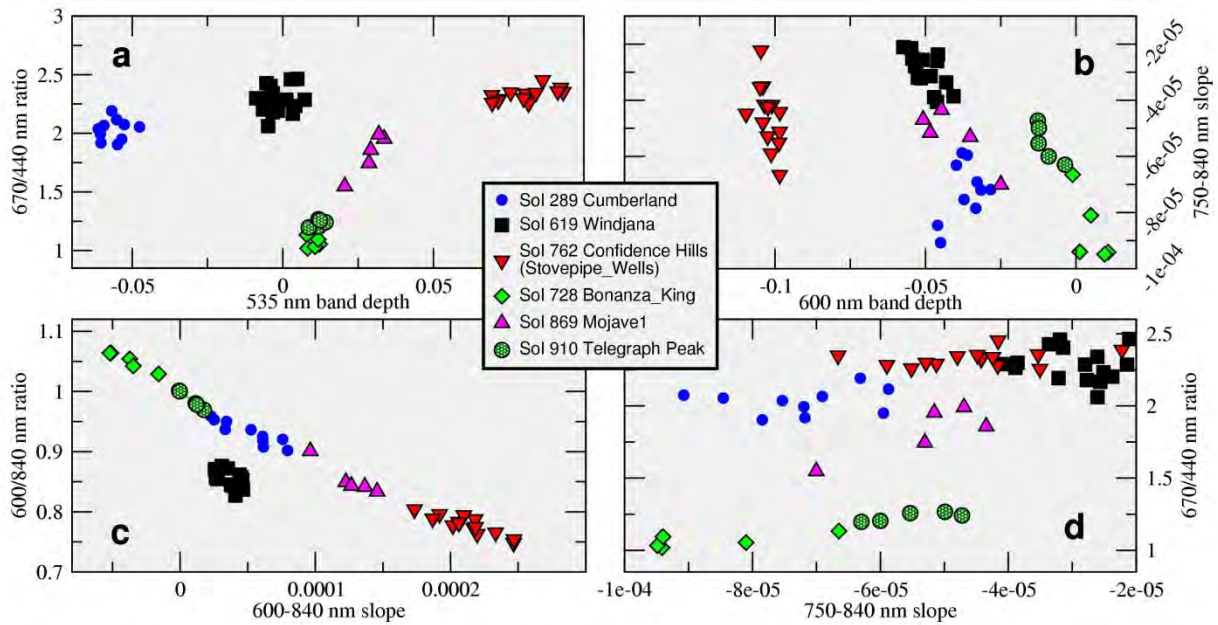
877
878 **Figure 11.** Spectral parameter comparisons for all drill tailing spectra. Not plotted is Perdido2
879 location #5, whose values of 750-840 nm slope ($-3.5e^{-4}$), 600/840 nm ratio (1.14), and 600-840
880 nm slope ($-1.1e^{-4}$) fall well outside the ranges plotted here.

881
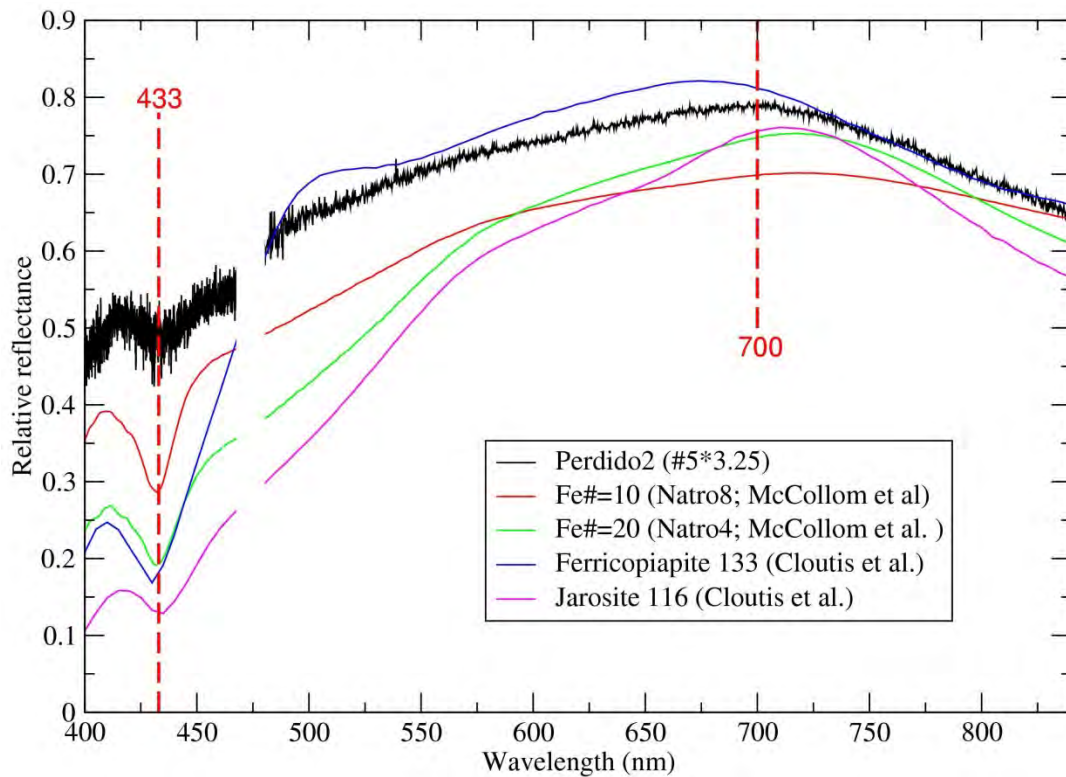
Figure 12. ChemCam passive spectrum of Perdido2 location #5 multiplied by 3.25 to facilitate comparison to laboratory spectra. Missing 468-480 nm data represents region between ChemCam detectors. Jarosite and ferricopiapite are from Cloutis et al. (2006) and synthetic natroalunite samples with small Fe# [= $100 \times$ Fe/(Al+Fe), molar basis] are from McCollom et al. (2014). The absorption near 433 nm, reflectance downturn shortward of 410 nm, and reflectance downturn longward of 700 nm in Perdido2 are consistent with the presence of these types of iron sulfate minerals.

890
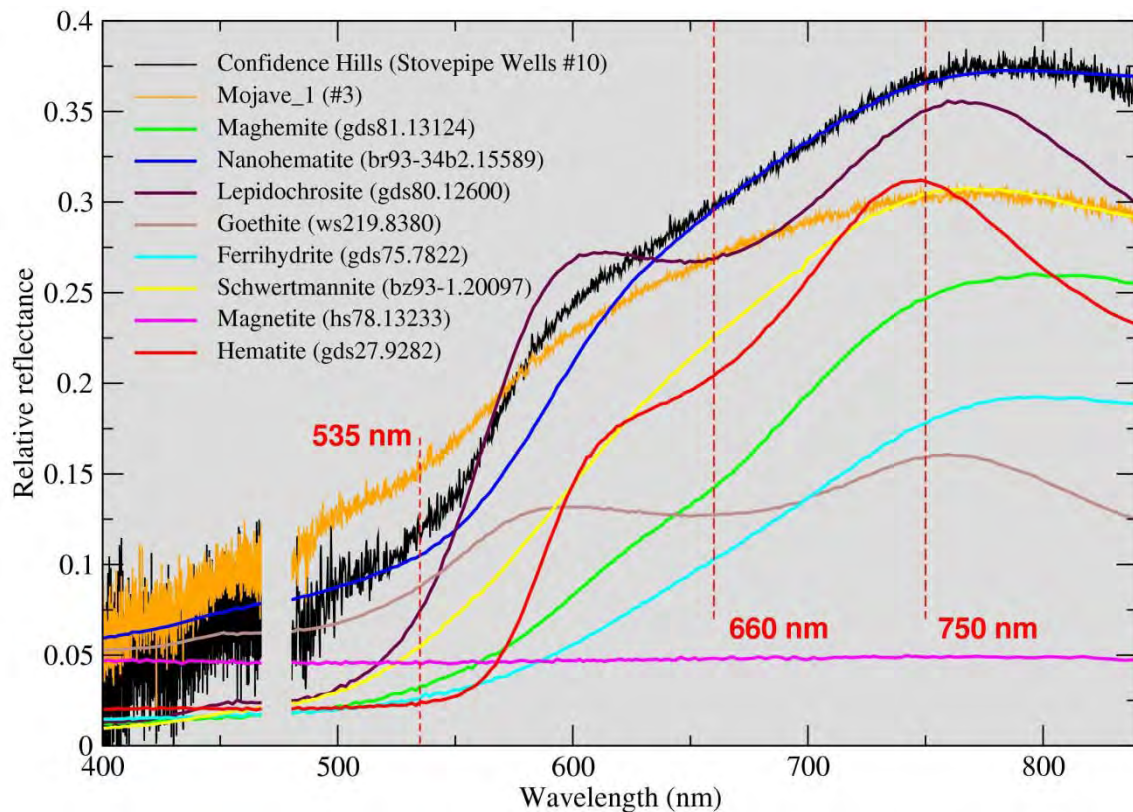
Figure 13. ChemCam passive spectra of Confidence Hills (Stovepipe Wells target location #10
from Figure 8) and Mojave drill tailings, contrast enhanced to facilitate comparison to laboratory
spectra of iron oxides. Missing 468-480 nm data represents region between ChemCam detectors.
Laboratory spectra are from USGS database (Clark et al. 2003). The combination of a broad
absorption near 535 nm, the flat, linear increase through the 660 nm region, and a decrease in
reflectance longward of 750 nm suggest the presence of a combination of crystalline and/or
nanophase hematite and a hydroxylated ferric phase like goethite or lepidocrocite.

47
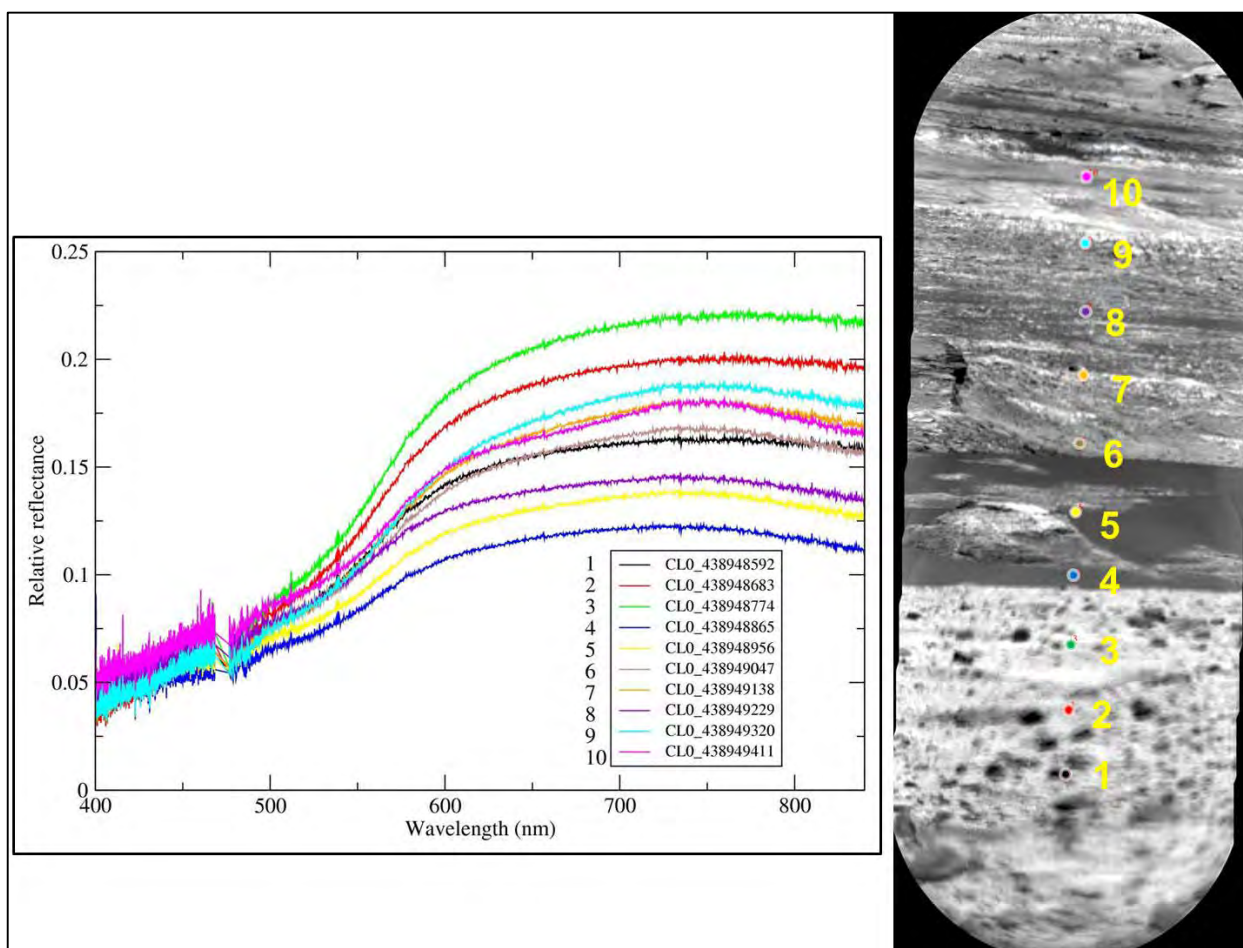
Figure 14a. ChemCam relative reflectance spectra (*left*) of Hematite Ridge 1 (HR1) area (cf. Figure 8) acquired on Sol 467 numbered according to acquisition locations shown in RMI mosaic (*right*). Colored points are located at approximate position and size of passive spectra fields-of-view, and color-coded to those in the spectral plot. Locations on Hematite Ridge (#6,7, 9, 10) show steep fall-off > ~747 nm, a weak band near 670 nm, and higher 535 nm band depth, consistent with hematite. Dark dune materials (locations #4,5,8) exhibit gradual fall-off > 750 nm consistent with olivine/pyroxene-bearing basaltic materials. Legend numbers correspond to spacecraft clock time used in CL0* filenames.
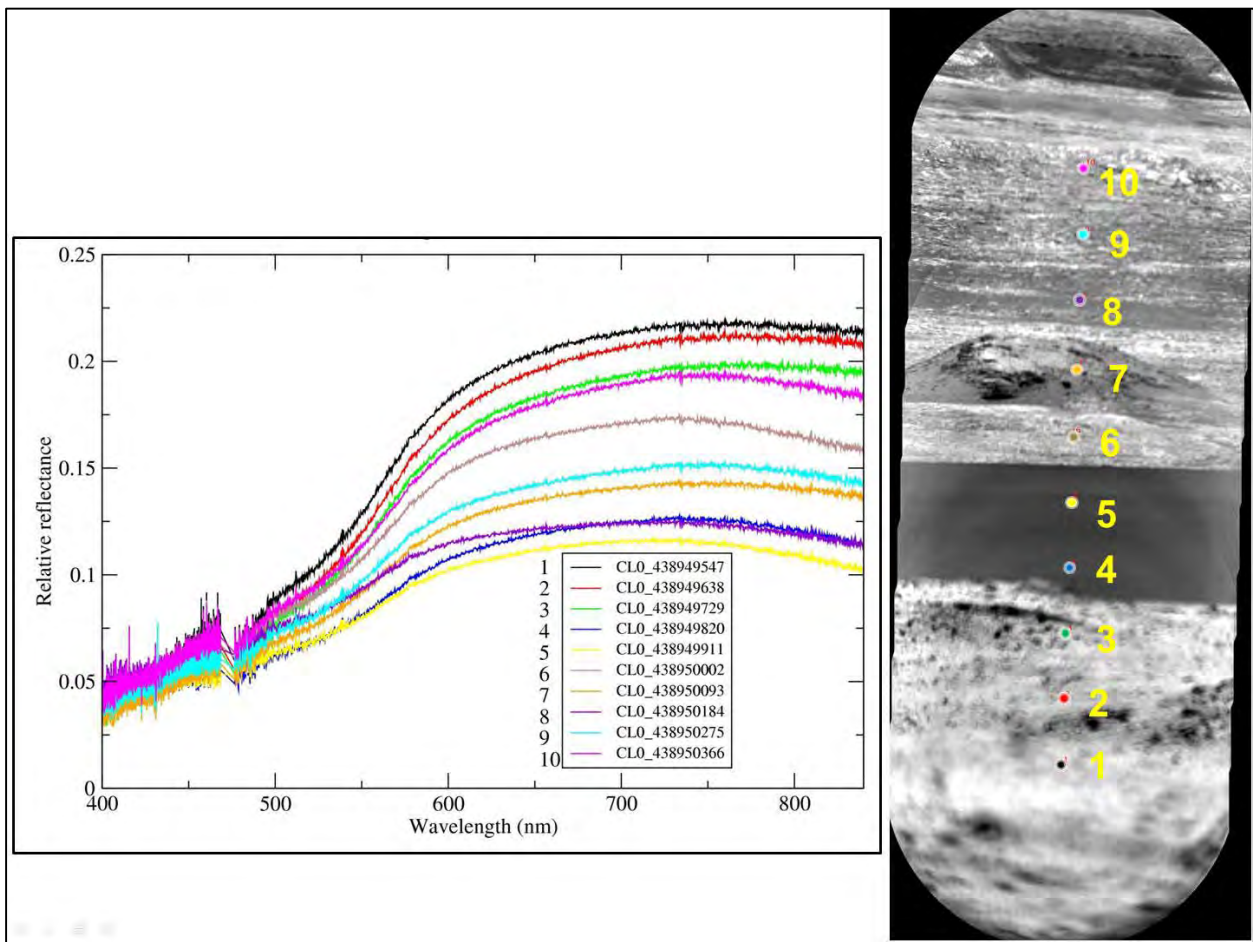
Figure 14b. ChemCam relative reflectance spectra (*left*) of Hematite Ridge 2 (HR2) area (cf. Figure 8) acquired on Sol 467 numbered according to acquisition locations shown in RMI mosaic (*right*). Colored points are located at approximate position and size of passive spectra fields-of-view, and color-coded to those in the spectral plot. Locations on Hematite Ridge (#6, #10) show steep fall-off > ~747 nm, a weak band near 670 nm, and higher 535 nm band depth, consistent with hematite. Dark dune materials (locations #4,5,8) exhibit gradual fall-off > 750 nm consistent with olivine/pyroxene-bearing basaltic materials. Legend numbers correspond to spacecraft clock time used in CL0* filenames.
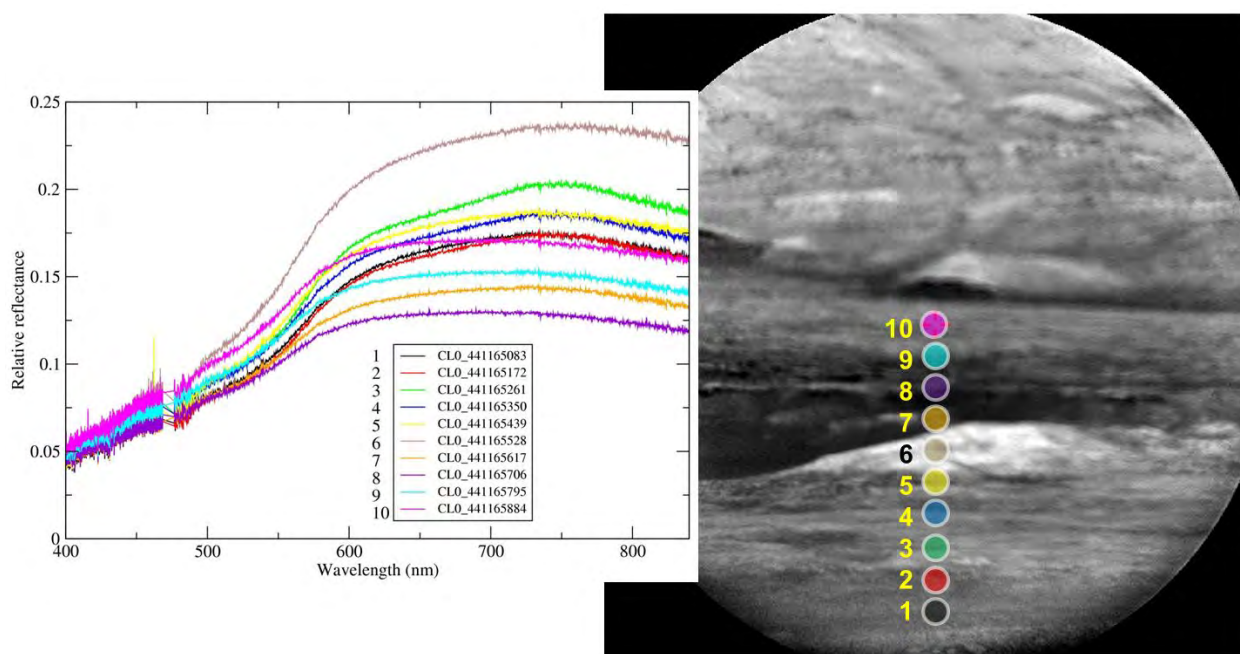
Figure 15. Sol 492 ChemCam passive spectra from raster HR5 acquired on Sol 492 and corresponding RMI image (CR0_441165845EDR_F0240408CCAM01492M1) of light-toned mound circled in Fig. 9. Colored points are located at approximate position and size of passive spectra fields-of-view, and color-coded to those in the spectral plot. Hematite-bearing regions are present on locations #3-5 (Hematite Ridge). Dark dune materials are present at locations #7-9, and location #10 on the "fan" materials exhibits similar spectral features at higher relative reflectance. Location #6 hit the light-toned mound but reveals few diagnostic spectral features in this wavelength range.

50
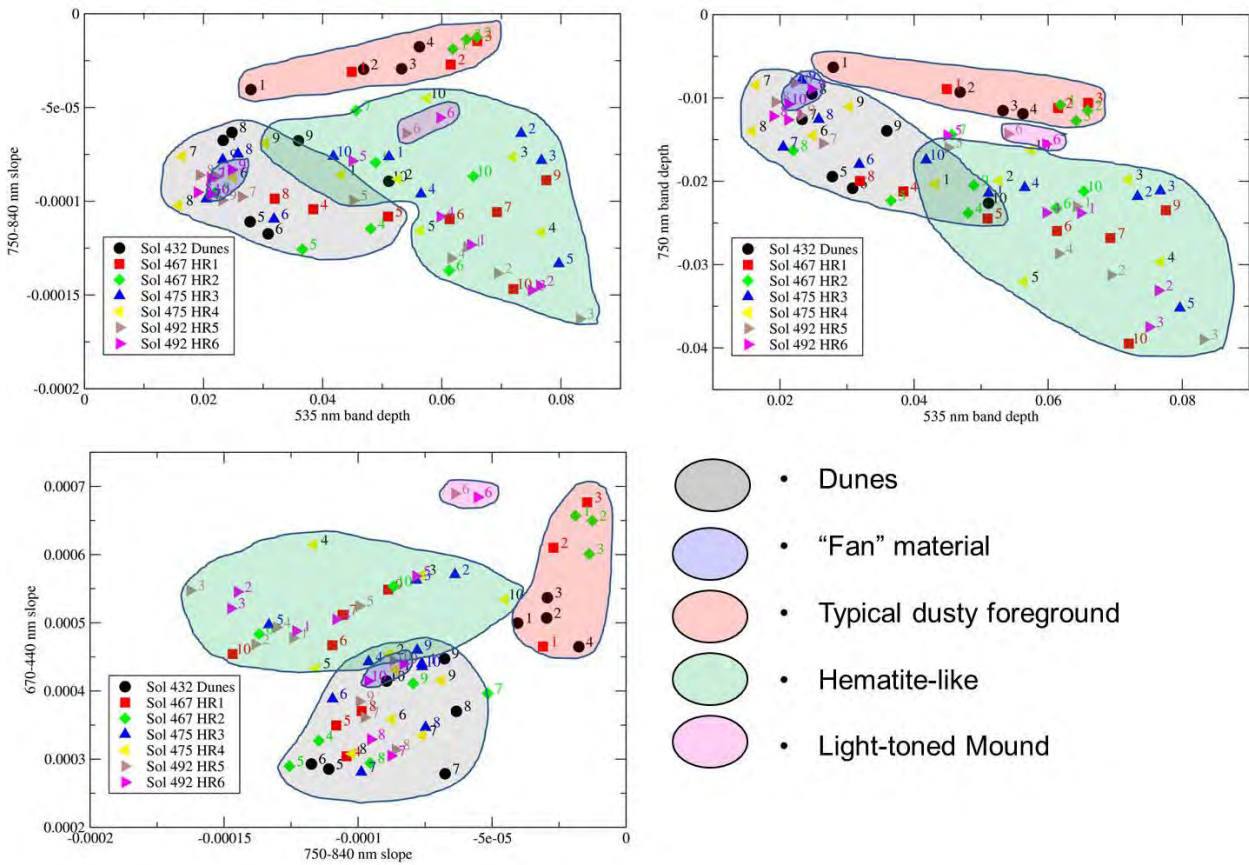
926

927 **Figure 16.** Representative spectral parameter plots for long-distance ChemCam passive spectra
928 (Table 1). Location numbers for each raster shown next to symbols (color-coded by
929 observation). Polygons show generalized spectral parameter regions associated with typical
930 dusty foreground materials, dunes, materials on the "fan" unit, the light-toned mound material
931 (Sol 492), and hematite-like spectra on or near Hematite Ridge.

932